Modeling the marginal ice zone in a coupled wave-ice model : insights from RADARSAT and CryoSat-2-derived floe size

BENJAMIN WARD, Department of Atmospheric & Oceanic Sciences

McGill University, Montreal

AUGUST, 2023

A thesis submitted to McGill University in partial fulfillment of the requirements of the degree of

Master of Science

Abstract

The shift toward a seasonal sea-ice cover has motivated scientific interest in the marginal ice zone (MIZ). The understanding of the processes at play in wave-ice interaction remains, however, rudimentary as coupled wave-ice models are poorly constrained by observations. Here, we couple the CICE sea-ice model to WAVEWATCHIII (WW3), including a prognostic equation for the floe-size distribution, a flexural ice-breaking scheme, and wave attenuation to simulate the MIZ extent using two definitions: floe size (MIZ-FSD) and sea-ice concentration (MIZ-SIC). We assess the realism of the simulated MIZ-FSD with comparison to the mean floe diameter derived from low-resolution (25 km) altimetric floe chord measurements (CryoSat-2) and higher resolution (10 km) RADARSAT synthetic aperture radar analysis from the Canadian Ice Service (CIS). When compared to CIS, the MIZ-FSD is shown to be overestimated by CryoSat-2 because of the lack of freeboard detection in the small floe range (0-1 km), in low-concentration regions and along the coastline. Then, results show that the simulated MIZ-FSD extent is systematically larger than the MIZ-SIC as the wave fracture affects the entire width of the MIZ-SIC in contrast to both of the observational datasets. Finally, we test the model's sensitivity to various wave attenuation schemes, showing that a strong floe-dependent attenuation is required to reproduce a more realistic MIZ-FSD by reducing wave-induced ice fracture and by increasing the formation of large floes in the pack. Those results point to the need for a universal wave fracture criterion and a better representation of the processes affecting the floe size distribution over the full observed floe range (0-10 km) to further improve the representation of the MIZ in fully coupled wave-ice models.

Abrégé

La transition vers un couvert de glace saisonnier est un facteur qui motive le besoin d'une meilleure compréhension des processus physiques qui sont en jeu dans la zone de glace marginale (MIZ). Ceux-ci demeurent largement méconnus puisque peu d'observations sont disponibles pour valider les modèles de vague et de glace couplés. Dans cette étude, un modèle de glace (CICE) est couplé à un modèle de vague WAVEWATCHIII (WW3). Un tel modèle comprend une équation prognostique pour la distribution de taille des plaques de glaces (floes), une représentation de la fracture de la glace soumise aux forces de flexions induites par les vagues ainsi qu'un schéma d'atténuation des vagues par la banquise. Deux définitions sont utilisées pour quantifier l'étendue de la MIZ, soit un critère basé sur la distribution de taille des glaces (MIZ-FSD) ou sur la concentration de glace de mer (MIZ-SIC). Les résultats sont ensuite validés au diamètre moyen des floes dérivés des mesures de deux satellites: CryoSat-2 basé sur les segments de floes détectés par un altimètre et RADARSAT basé sur l'analyse d'images radar produites par le Service canadien des glaces (CIS). Les données montrent d'abord que l'étendue de la MIZ-FSD est surestimée par CryoSat-2 en comparaison avec les données du CIS en raison d'un déficit de détection dans l'intervalle des floes de petite taille (0-1 km), dans les régions à faible concentration et le long de la côte. Ensuite, l'étendue de la MIZ-FSD simulée est systématiquement plus grande que celle de la MIZ-SIC, car la fracture des vagues affecte toute la largeur de la MIZ-SIC, contrairement à ce qui est reporté dans les observations. Finalement, l'étude de la sensibilité du modèle à une variété de schémas d'atténuation des vagues montre qu'une forte atténuation dépendante de la taille des

floes est nécessaire pour reproduire une MIZ-FSD plus réaliste, car une forte dissipation entraine une réduction de la fracture et une augmentation de la génération de gros floes dans la banquise. En conclusion, une meilleure représentation de la MIZ pourrait être obtenue par le développement d'un critère universel de fracture ainsi que par une représentation des processus affectant la distribution de taille des glaces couvrant toutes les échelles de taille.

Acknowledgements

Mon grand-père était conseiller en orientation : l'éducation est donc une valeur qu'il avait à coeur. D'ailleur, comme cadeaux d'anniversaires il préférait placer de l'argent dans un régime d'épargne d'étude. C'est entre autres grâce à lui que j'ai eu le privilège de choisir et de poursuivre mes études dans un domaine qui me passionne. Quand j'ai commencé ma maîtrise, il m'a montré fièrement le brouillon de sa propre thèse, un vieux document papier griffonné en rouge de commentaires indéchiffrables par son superviseur, me rappelant qu'il y a des choses qui ne change pas. Mon grand-père est décédé le 23 octobre 2022. Faute de pouvoir lui faire lire à mon tour le fruit de mon travail, je lui dédis cette thèse, car sans lui, rien n'aurait été possible. Merci pour tout papy xxx.

Je remercie mon superviseur Bruno Tremblay pour son encadrement, mais aussi pour sa confiance et le caractère exploratoire de ce projet. Je suis aussi reconnaissant de sa patience, de son cerveau bouillonnant d'idée, des opportunités qui m'ont été offertes et de ses passes sur la palette.

I would also like to extend my thanks to Lettie Roach, Denise Sudom, Jean-Francois Lemieux, Dany Dumont, Alain Caya, and David Straub for their valuable insights, Philippe Blain and Jérémy Beaudry for their patient guidance with CICE and WW3, and my colleagues from the sea-ice group for their support.

Finalement, je remercie ma famille, mes amis, mais surtout celle qui m'a accompagné tous les jours, mon amoureuse Anne-Marie Sauvageau, sans qui ces deux années auraient été nettement plus pénibles.

Table of Contents

Chapter 1

Forward

This Master's Thesis will be adapted to a paper that will be submitted to the Cryosphere Journal in the Fall of 2023. The paper will exclude the last result section regarding the thermodynamic and dynamic effect of the coupling. The final paper will be subject to changes compared to this version following a round of internal review by the co-authors and a round of external review after submission to the journal.

All of the required elements for a thesis are included: an introduction with a comprehensive review of the literature, a description of the models and the data used for validation, and a presentation of the leading research findings with a comprehensive scholarly discussion and conclusion. The wave-ice model (WIM) coupler, as well as the CICE/WW3 source codes, namelists, and configurations, are publicly available at `https://github.com/bward-mcgill`.

1.1 Manuscript information

Title: Modeling the marginal ice zone in a coupled wave-ice model: insights from RADARSAT and CryoSat-2-derived floe size.

Authors: Benjamin Ward (BW), Bruno Tremblay (BT), Lettie Roach (LR), Denise Sudom (DS), Jean-Francois Lemieux (JFL), Dany Dumont (DD) and Alain Caya (AC).

1.2 Author and Co-authors contributions

BW designed and coded the coupler for the models and performed the simulations. BW conducted the literature review, performed the analysis, and wrote the manuscript. BT participated in the writing of the manuscript and supervised the research. DS and BT participated in monthly discussions. LR, JFL, and DD reviewed, provided corrections, and contributed to formulating the research question and methodology. AC provided the RADARSAT-derived ice chart data from the Canadian Ice Service and reviewed the manuscript.

Chapter 2

Introduction

The increase in greenhouse gases concentration is inducing a radical metamorphosis of the Arctic sea-ice cover with a warming signal four times higher in the Arctic than the global average (e.g. Rantanen et al., 2022). Of particular interest are the record in the minimum sea-ice extent of 2007 and 2012 (e.g. Perovich et al., 2008; Parkinson and Comiso, 2013) and the transition from old multi-year sea ice to a much younger ice-covered ocean with mainly first- and second-year ice (e.g. Kwok, 2018; Stroeve and Notz, 2018). While there is still uncertainty concerning the mechanisms that are driving the observed multi-year ice loss (e.g. Overland and Wang, 2013; LeGuern-Lepage and Tremblay, 2022) and a large intermodel variability (e.g. Wang and Overland, 2012; Shu et al., 2020), the scientific consensus is that the Arctic will be seasonally ice-free in a few decades (Jahn, 2018). These changes in the sea-ice cover have led to an increased scientific interest in the area of transition between the open ocean, and the pack ice called the marginal ice zone (MIZ), where surface gravity waves affect the ice cover by breaking the ice into smaller fragments called floes.

The transition to a seasonal sea-ice cover is characterized by a widening of the MIZ inherent to a thinner, younger, and more mobile (i.e., more ”MIZ-like”) sea-ice cover in conjunction with an increased area of open water in the summer where longer fetch leads to waves with larger amplitude that penetrate deeper in the pack ice (e.g. Thomson and Rogers, 2014; Li et al., 2019). This positive feedback is projected to amplify with an increase in intensity and frequency of storms at high latitudes (e.g. Liu et al., 2016; Casas-Prat and Wang, 2020) leading to large sea ice losses (e.g. Asplin et al., 2012; Browne et al., 2017). Using satellite-derived sea ice concentration, Strong and Rigor (2013) showed an increase in the observed MIZ area in the last decades; however, current Earth system models have a poor representation (if any) of wave-ice interaction and fail to reproduce this regime transition.

Sea-ice interactions with waves are a crucial component in multiple feedbacks at play in the transition to the seasonal Arctic. During the melting season, wave-induced fracture creates smaller floes, increases lateral melt, and reduces sea-ice concentration leading to longer fetch, lower attenuation, and deeper penetration of incoming waves (Casas-Prat and Wang, 2020; Asplin et al., 2014; Horvat, 2022). Conversely, a potential competing effect exists as the attenuation of the waves transfers momentum to the ice, generating additional stress and compacting the ice, which attenuates the wave even more (Auclair et al., 2022). Horvat (2022) also discusses another negative feedback, in fall and winter, as wave-induced fracture promotes ice growth in sea-ice leads and damps waves, allowing the ice cover to strengthen even more. These retroactions have essential implications on short time scales (e.g., sea-ice forecast, navigation, offshore oil industry) and decadal time scale (e.g. Asplin et al., 2014; Kohout et al., 2014; Tsamados et al., 2015).

Since the seventies, key advancements have been made in the field of wave-ice interaction, including a better understanding of 1) the processes affecting the statistical distribution of floe size, 2) the wave-induced flexural fracture of floes, 3) the attenuation of waves in the MIZ that is closely linked with 4) the momentum transfer from ocean waves. Nevertheless, fully coupled wave-ice models referred to as the *Holy Grail* of MIZ research (Squire, 2022), remain embryonic, as not many observational data are available to constrain the parameterization.

The floe-size distribution (FSD) in the MIZ range from centimeter scale (newly formed pancake ice) to hundreds of meter scale (large floes broken by swells) (e.g. Toyota et al., 2006; Alberello et al., 2019). In the pack ice, floes are delineated by linear kinematic features, and the typical floe size can range up to tens of kilometers wide (e.g. Perovich and Jones, 2014; Stern et al., 2018). A recent approach involves solving a prognostic equation for the joint floe size and thickness distribution (FSTD). In the MIZ, the FSTD evolves due to thermodynamical and mechanical processes (i.e., lateral melt/growth and welding) as well as wave-ice interaction processes (i.e., wave fracture and new ice formation) represented as parameterized source/sink terms function of wave height, wavelength and ocean temperature (Horvat and Tziperman, 2015; Zhang et al., 2016). In the pack ice, the FSTD equation evolves via mechanical processes only (i.e., ridging and rafting) that affect the thickness distribution but not the floe size.

Wave-induced sea ice fracture associated with flexural stresses was first parameterized based on two limits: a maximum strain failure criterion assuming that the ice is a thin elastic plate that follows the ocean surface and a maximum stress failure criterion assuming that the ice is a rigid plate subjected to buoyancy and gravity forces (Dumont et al., 2011). The ice is considered to break if one of the two failure criteria is met in a wavelength range between $\approx$ 40-400 m, and the resulting maximum floe size depends on the wavelength. From the extremums of the distribution, they use a probabilistic method based on the power-law formalism of Toyota et al. (2011) to retrieve the FSD. Later, Williams et al. (2013) eliminated the stress criterion arguing that a bending moment on a non-deforming ice floe that increases with wavelength could lead to unphysical wave fracture even by low amplitude long wavelengths deep into the pack and a much broader MIZ. The strain criterion alone has now become standard in the community (e.g. Williams et al., 2017; Boutin et al., 2018; Horvat and Tziperman, 2015). This criterion can, however, leads to an unrealistically large strain associated with high-frequency (short wavelength) that can exceed the critical threshold, particularly in the areas where the ice is the thickest (recall that the maximum tensile stress in a plate is linearly related to the ice thickness), even if the waves are of small amplitudes (e.g. Cooper et al., 2022).

Wave height (or energy) decreases exponentially in the MIZ with a preferential attenuation for high frequency (short wavelength) waves through scattering and dissipation (e.g. Squire and Moore, 1980; Wadhams et al., 1988). Scattering is stronger for wavelengths that are comparable to the floe size and is a conservative process: wave energy is reflected/transmitted at each floe interface in different directions and frequency (e.g. Squire, 2007; Montiel et al., 2016; Meylan and Bennetts, 2018; Meylan et al., 2021). Dissipation, on the other hand, is non-conservative and operates through basal friction, inelastic dissipation, collisions between floes, floe breaking, and many other processes (e.g. Boutin et al., 2018; Squire, 2020). Two theory-based dissipation models are commonly used in the community to represent the complexity of these various processes: the thin elastic plate theory (Liu and Mollo-Christensen, 1988) or the viscoelastic theory (Keller, 1998). Up until now, none of the models proposed can fully explain observations as dissipation is a combination of all the above-mentioned processes (and likely others) depending on the wavelength and type of ice (e.g. Collins et al., 2017; Shen, 2019, 2022). For this reason, attenuation schemes were recently derived from an empirical fit to data collected from wave buoys deployed in the MIZ (e.g. Meylan et al., 2014; Rogers, 2017).

As they are attenuated, waves exert a normal force on the draft of ice floes (i.e., form drag), hereby referred to as wave-radiation stress (WRS), caused by the exchange of momentum between the waves and ice (e.g. Longuet-Higgins and Stewart, 1964). In current models, the wave momentum is assumed to be only transferred to the ice (and not to the ocean/atmosphere) for simplicity, providing an upper bound to the WRS (Auclair et al., 2022). Using Sentinel-1 synthetic aperture radar measurement Stopa et al. (2018) showed that the WRS could be of a similar order of magnitude or even larger than the wind stress in the MIZ. Sutherland and Dumont (2018) used a simple equilibrium model to derive a length scale (tens of kilometers) for which the WRS is dominant compared to wind stress. In such a region, the WRS can increase thickness by 1-2m and sharpen the ice edge (Liu et al., 1993; Sutherland and Dumont, 2018). Additionally, Auclair et al. (2022) showed that the effect of the WRS is the result of a complex balance of force that is highly sensitive to the ice strength and the wave attenuation formulation using a 1-D wave-ice model.

Early coupled wave-ice models were unidimensional and included wave scattering, floe breaking, and a diagnostic equation for the FSD (Dumont et al., 2011; Williams et al., 2013). Later, Williams et al. (2017) coupled a two-dimensional wave model to the neXtSIM sea-ice models, including the WRS. Recently, Boutin et al. (2020) coupled the WAVEWATCHIII wave model (WW3) to the LIM3 sea-ice model on a pan-Arctic domain, considering a refined version of the thin-elastic plate dissipation formulation including scattering and inelastic/anelastic dissipation, that was later validated against CryoSat-2 measurements (Boutin et al., 2018, 2022), as well as an FSD equation based on Zhang et al. (2016), where the evolution of thickness and floe size are independent (instead of an FSTD). They conclude that wave-ice interaction significantly impacts the position of the ice edge at a short time scale. In Boutin et al. (2021), the effect of the WRS is revisited using a coupled WW3 and neXtSIM sea-ice model where the effect of waves on the damage parameter is considered by weakening ice strength in highly fractured areas using two different floe-size distributions (i.e., a fast growth and a slow growth) that evolves in parallel to allow for the ice to keep a memory of the previous fragmentation. The wave fracture scheme remains, however, rudimentary as it assumes a power-law formalism for redistributing the areal fraction in each floe-size category. In Boutin et al. (2020, 2021), the focus is placed on specific cases in the Beaufort and Barent Seas, but no comparisons between the simulated and observed mean floe diameter (MFD) are provided for these specific events.

In parallel, development was made by the CICE consortium to include the effect of waves in their coupled ice-ocean models (CICE). Roach et al. (2018) included a joint floe-size thickness distribution (FSTD) based on the equation of Horvat and Tziperman (2015), allowing for the FSD to emerge naturally from wave-ice dynamics without assuming a priori shape of the FSD. The authors report on a realistic seasonal cycle in the Arctic and the Antarctic using 12 floe size categories, however, without comparison to observations. Later, they proposed a wave-dependent ice formation formulation based on the tensile failure limits for pancake creation and successfully reproduced an increase in the lateral melt due to wave-ice feedback at a seasonal timescale using a fully coupled version of CICE and WW3 with a daily exchange of variables (Roach et al., 2019). In Horvat et al. (2019), a first comparison of the coupled wave-ice model against observation is made with the pan-Arctic CryoSat-2-derived MFD by increasing the number of floe size categories to 24 in the model to cover the 0-10 km floe size range. However, the FSD model is developed for the MIZ floe size range (0-1 km), an interval of floe size poorly resolved by the satellite, making any direct MFD comparison questionable. A recent sensitivity study using different empirical attenuation schemes with an increased (hourly) coupling frequency showed that enhanced wave generation was required to reproduce the wave spectrum observed by buoys in the Beaufort Sea (Cooper et al., 2022). The realism of the simulated FSD compared to observation, however, was not addressed, except for noting that the choice of attenuation schemes significantly impacted the MFD.

Here, we use the same coupled CICE-WW3 slab ocean model with an hourly coupling frequency but now consider WRS from a wide range of attenuation formulations. We focus on the simulated MFD and provide a comparison to CryoSat-2 observations and the analysis of RADARSAT images from the Canadian Ice Service (CIS). The paper is structured as follows: Section 5.1 discusses the biases associated with CryoSat-2 compared to CIS-derived MFD in the Labrador/Baffin Bay region. In Section 5.2, we validate the simulated floe size, first in the Labrador region, where the two observational datasets are available, followed by a pan-Arctic comparison with CryoSat-2 - the only dataset available for the entire Arctic. Section 5.3 investigates the sensitivity of the coupled wave ice model to a range of attenuation formulations, providing further insight into the intricate balance of FSD processes. Section 5.4 discusses the effect of the thermodynamic (lateral melt) and dynamic (WRS) effects of the coupling at seasonal and daily timescales but will not be included in the final publication.

Chapter 3

Coupled model components

We couple the CICE consortium sea-ice model version 6.4.1 (CICE) (Hunke et al., 2022b), with the column physic model Icepack version 1.3.3 (Hunke et al., 2022a) and the two-dimensional ocean surface wave model WAVEWATCH III® version 6.07 (WW3) (WW3DG, 2019). CICE solves the two-dimensional momentum balance equation for sea ice :

$$m\left(\frac{\partial \mathbf{u}}{\partial t} + f \times \mathbf{u}\right) = \mathbf{F_{tot}} + \nabla \cdot \sigma \tag{3.1}$$

where m is the combined mass of ice and snow per unit area, $\mathbf{u}$ the velocity vector, f the Coriolis parameter, $\mathbf{F_{tot}}$ the external stress (i.e., surface wind stress, ocean stress, sea-surface tilt, and wave-radiation stress) and $\nabla \cdot \sigma$ the divergence of the internal stress tensor (σ_{ij}) - representing the mechanical properties of the sea ice. The temporal evolution of state variables (e.g., thickness, concentration) is made by a third-order advection scheme, and the thermodynamic source terms are calculated in the vertical physics module Icepack (Hunke et al., 2022a). The model physics incorporated in Icepack most notably include the mushy layer thermodynamic with evolving salinity (Feltham et al., 2006; Turner et al., 2013), level-ice melt ponds (Hunke et al., 2013), and a joint floe-size thickness distribution (FSTD) (Roach et al., 2018).

WW3 predicts the temporal evolution and propagation of the wavelength-direction energy spectra ($E(\lambda, \theta)$). The spectral and directional domains are discretized into 20 frequency categories (covering the $\approx$ 0.04-0.25 Hz frequency range) and 24 direction categories (i.e., directional resolution of 15^o). In the absence of underlying currents, the wave energy obeys a conservation equation of the form :

$$\frac{DE}{Dt} = S_{in} + S_{nl} + S_{ds} + S_{ice} + ... \tag{3.2}$$

where S_{in} is the wave growth due to wind, S_{nl} is the nonlinear resonant wave-wave interactions, S_{ds} the dissipation due to white capping, and S_{ice} the wave attenuation by sea ice (WW3DG, 2019). When ocean currents are considered, the same equation applies with the wave energy spectra replaced by the wave action instead.

3.1 Joint Floe-Size Thickness Distribution (FSTD)

The joint floe size and thickness distribution (FSTD) of Horvat and Tziperman (2015) can be written as:

$$\frac{\partial f(r,h)}{\partial t} = -\nabla \cdot f(r,h)\mathbf{u} + \mathcal{L}_T + \mathcal{L}_M + \mathcal{L}_W \tag{3.3}$$

where, $f(r,h)$ is the ice areal fraction of ice in a given floe size (r) and thickness (h) category, $\mathcal{L}_T$ are the floe size tendency terms due to thermodynamic effects including new ice formation, lateral growth, lateral melt and welding of existing floes. $\mathcal{L}_M$ and $\mathcal{L}_W$ are the mechanical effects (i.e., ridging and rafting) and the redistribution effect caused by wave fracture. Note that the floe-size distribution (FSD), the ice thickness distribution (ITD), and the total ice concentration are the integrals of the FSTD over for all thicknesses, floe sizes, or both respectively (Roach et al., 2018). In the above equation, the thermodynamic effects only affect the FSD, while the mechanical effect only affects the ITD. The reader is referred to Horvat and Tziperman (2015); Roach et al. (2018, 2019) for more details on the exact formulation of $\mathcal{L}_M$ and $\mathcal{L}_T$. The redistribution of floes by ocean waves between floe size categories ($\mathcal{L}_W$) is made using the machine learning model of Horvat and Roach (2022). The algorithm was trained on the physical floe breaking superparameterization of Horvat and Tziperman (2015) given by :

$$\mathcal{L}_W = -\Omega(h, r) + \int_0^{\infty} \Omega(h, r')\beta(r, r', h)dr' \tag{3.4}$$

where $\Omega(h, r)$ is the rate at which the fractional area of a given floe size (r) and thickness (h) decreases because of the wave fracture and $\Omega(h, r')$ is the rate at which the fractional area of floes larger than r' breaks, and $\beta(r, r', h)$ represents the probability that a floe larger than r' breaks into a floe of size r. These fracture rates and probability are derived from a realization of the sea-surface height with an incident wave spectrum and a random phase. The axial strain at the ice surface is then computed from each triplet of extrema (min, max, min), assuming that ice always deforms perfectly with sea-surface height and the strain criterion derived in Dumont et al. (2011) is used to determine a set of points where the fracture occurs given the ice thickness. This point set is used to create a fracture histogram, and realizations of the sea-surface height are generated with new random phases until the convergence of two subsequent fracture histograms occurs.

The heavy computing cost required for the convergence of this superparameterization remains a major drawback compared to simpler floe-breaking schemes based on the power-law formalism (e.g. Williams et al., 2013; Boutin et al., 2018). The AI-based fracture model used in this study has been trained from wave spectrum inputs and reproduces the fracture histogram outputs accurately from the physical fracture model with reduced computing cost (Horvat and Roach, 2022). Note that to reduce the false negative rate, the machine learning model has been only with waves of a significant height larger than 0.1 m, which conveniently removes most of the small locally generated high-frequency waves that lead to an unrealistic floe fracture from the strain criterion.

In the FSTD model, we consider 12 floe size and 5 thickness categories ranging from 0 to 1 km and 0 to 4.5 m, respectively. In the central Arctic, larger floes (≈ 10 km) are fractured by other processes, such as linear kinematic features. These are not considered in the FSTD, and as such, while the ITD model is applicable for the entire Arctic, the FSD model is only valid in the MIZ. Note that another configuration has been proposed by Horvat et al. (2019), using 24 FSD categories, with the largest category being 33 km to cover the full range of observed floe size. However, we are bound to use 12 FSD categories as the machine learning fracture scheme is trained with this specific configuration.

3.2 Wave attenuation and generation

To represent a wide range of attenuation, we performed sensitivity simulations considering two in-situ data (empirical) and two theory-based dissipation (IC) and scattering (IS) parameterizations (see table 3.1). Both theory-based dissipation schemes are used jointly with the floe-size dependent scattering scheme (IS2) of Meylan and Masson (2006) where the scattering, valid for short wavelengths, is represented by a linear Boltzmann equation. Empirical attenuation schemes (IC4) are derived from measurements in the field and, therefore, already include scattering.

Model runs	Attenuation schemes	Reference
IC4-M3 (CTRL)	Empirical thickness-dependent	Kohout and Meylan (2008)
IC4-M8	Empirical floe-size dependent	Meylan et al. (2021)
IC2/IS2	Theory : thin elastic plate	Boutin et al. (2018)
IC5/IS2	Theory : visco-elastic	Mosig et al. (2015)

Table 3.1: List of the simulations performed in this study using different scattering/dissipation parameterization.

The empirical formulation IC4-M3, which accounts for frequency and thickness dependencies, serves as the control model in this study as it has been the configuration of choice used in the first implementations of the FSTD in CICE (Horvat and Tziperman, 2015; Roach et al., 2018). It is based on a fit to an attenuation coefficient derived from measurement for short/medium wavelengths and large floes of a thickness between 0.5 to 3 m that has been interpolated to cover the full range of thickness and frequency (Kohout and Meylan, 2008). The IC4-M8 is fit to wave attenuation observation by Meylan et al. (2021) where a scattering model is used to reproduce attenuation for short wavelengths combined with additional damping for long wavelengths that is not accurately represented by the scattering theory. In contrast with IC4M3, IC4M8 is thickness and floe size-dependent with a stronger attenuation for small floes and has been used in the fully coupled wave-ice model of Roach et al. (2019) and Cooper et al. (2022).

The IC2 dissipation scheme, on the other hand, is derived from the thin elastic plate theory, where dissipation primarily arises from either molecular viscosity in the laminar ocean or eddy viscosity in a turbulent boundary layer. It is combined with the floe-dependent IS2 scattering scheme, and additional creep-based dissipation is added as it depends critically on the floe size (Boutin et al., 2018). We use the same parameters (e.g., under-ice viscosity, roughness length, flow law parameter) as the reference simulation (REF) of Boutin et al. (2022), which has been validated to IceSat-2 pan-Arctic wave in ice measurements. The IC5 dissipation scheme is also theory-based but derived from the viscoelastic layer models proposed by Fox and Squire (1994) and has demonstrated comparable performance to another viscoelastic layer model presented by Wang and Shen (2010) (known as IC3 in WW3), but with lower computational costs. We use the same parameters (i.e., effective viscosity, shear modulus, and ice density) as in (Mosig et al., 2015), a configuration that has been validated to wave measurement in the Antarctic MIZ.

.

The generation of waves (S_{in}) includes a linear contribution, which allows for the growth of small capillary waves, and a non-linear contribution, responsible for the growth of waves of larger amplitude. The configurations used in this study are the same as the one used in (Boutin et al., 2022) and have been validated against CryoSat-2 measurement in the open ocean. Both contributions are scaled by fractional area uncovered by sea ice (1-SIC). This scaling allows for small but non-zero wave generation events in nearly entirely ice-covered regions (SIC $\approx$ 1). While (Cooper et al., 2022) showed that this locally generated high-frequency wave exists, here we cap the scaling term to a minimum concentration of 0.8 in order to eliminate the unrealistic breakage of floes by high-frequency waves resulting from the strain floe breaking criterion within the pack ice.

3.3 Wave radiation stress (WRS)

The wave attenuation term (S_{ice}) is directly related to the wave radiation stress (WRS) as it is responsible for the transfer of momentum from the wave to the ice. In the most general case, WRS is a complex two-dimensional tensor as a function of the wave incident angle θ. In the MIZ, it is reasonable to assume a linear wave regime in a steady state where energy dissipation by sea ice is dominant compared to the other terms that modify the wave field (see equation 3.2). The WRS can then be approximated as the divergence of the WRS tensor in the same manner as for the internal ice stress tensor (Longuet-Higgins and Stewart, 1964). For waves traveling in the x-direction, the stress transferred to the ice by the wave field is :

$$\tau_{wvx} = -\rho_w g \left(E_0 e^{-\alpha x} \left[\frac{2c_g(x)}{c(x)} - \frac{1}{2} \right] \right) \tag{3.5}$$

where E_0 represent the initial incident energy, α is the attenuation coefficient in the direction perpendicular to the ice edge (dependent on the attenuation scheme used) and c_g and c are the group and phase speed of the waves.

3.4 Configurations

The most recent version of CICE (after the development of the FSTD in Roach et al., 2018) includes a partial coupling between the sea-ice momentum balance and the column physics by reading WW3 hindcast spectrums. In such a framework, the coupling is unidirectional: the wave spectrum is prescribed, and a resulting change in ice conditions does not feedback into the wave model. As in Roach et al. (2019), we implement a two-way sequential coupler, but for simplicity's sake, both the sea ice and the wave models are run successively with input/output. At each coupling timestep, we give the former output to the latter, and it is read as a forcing, allowing for a change in ice conditions to affect the wave conditions and vice versa (a summary of the variable flow is given in Fig. 3.1). Both model's time steps and the coupling frequency are set to 3600 s to represent short timescale feedbacks between the FSTD, the WRS, and the wave attenuation as in Cooper et al. (2022). Initial conditions come from a CICE model spin-up consisting of 9 years without FSTD in order to reach a steady state in sea-ice thickness and concentration, followed by a year of coupled model spin-up, where we initialize the FSD with the power law of Perovich and Jones (2014).

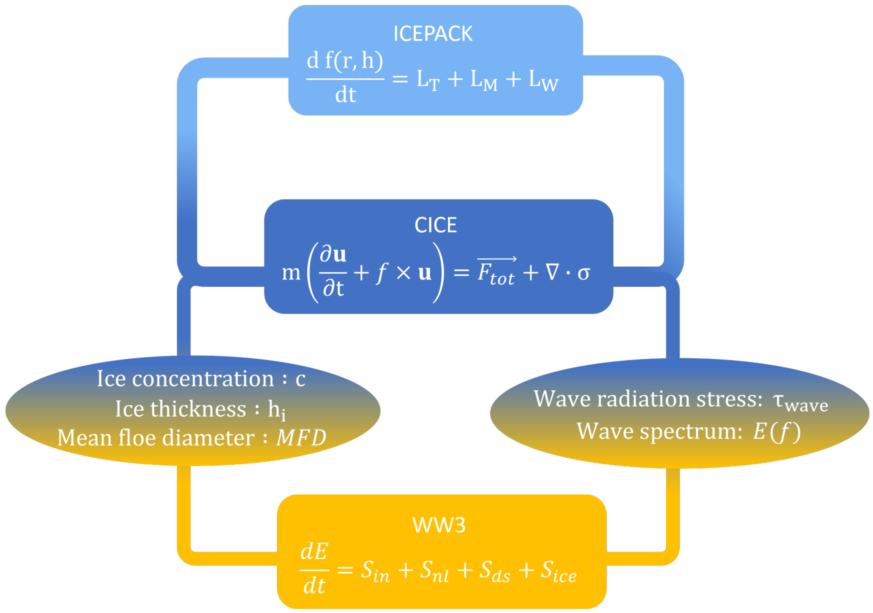

Figure 3.1: Variable flow for one timestep in the sequential two-way coupled WW3/CICE.

We use CICE and WW3 on a pan-Arctic configuration with a rotated pole curvilinear grid and a nominal horizontal resolution of 1^o. This configuration make use of the JRA-55 reanalysis for atmospheric forcing for both of the sea ice and the wave components (Kobayashi et al., 2015), a slab ocean model - independent of the wave component - where climatological values for temperature, salinity, mean current and heat/salinity flux below the mixed layer are prescribed from a Community Earth System Model Large-Ensemble (CESM-LE) control run (Kay et al., 2015) and a mixed layer parameterization where the surface temperature evolve prognostically (Bitz et al., 2012). Note that a number of default settings for CICE and WW3 are used, the reader is referred to the respective namelists for more information about all the model physics and parameters used.

Chapter 4

Observational data of the MIZ

4.1 Sea-ice concentration : NSIDC

We use the monthly National Snow and Ice Data Center Climate Data Record (NSIDC-CDR) mean sea-ice concentration (SIC) on a 25 km x 25 km equal-area scalable Earth (EASE) grid for the 1978-2021 time period derived from SMMR, SSM/I, and SSMIS passive microwave radiometer on the Nimbus-7 satellites (DiGirolamo et al., 2022). The SIC-based MIZ (MIZ-SIC) is traditionally defined as the region bounded by the ice edge and the close ice, characterized by sea-ice concentrations ranging from 0.15 to 0.8 (e.g., Strong, 2012). Mean errors in passive microwave SIC are around 5 % - 10 % but vary spatially and temporally, often reaching values of 30 % - 35 % during the melting season (with both under and over estimates) due to melt ponds, clouds, wet snow, coarse-grained snow, thin ice, or refrozen surfaces that influence sea-ice properties and introduce biases in the SIC retrieval algorithms (Kern et al., 2020).

4.2 Floe-size: CryoSat-2

We use the monthly mean floe-size dataset derived from 11 million CryoSat-2 floe chord measurements (i.e., geographic distance covered by a continuous series of points identified as sea ice by the satellite) for the winter periods of 2010 to 2018, gridded on a 25 km polar stereographic grid (Horvat et al., 2019). The FSD is derived from the floe chord, assuming a circular geometry. No FSD data is available over landfast (shoreward of the flaw lead polynya) and landlocked ice in the winter and the whole Arctic in the summer because satellite measurement cannot distinguish between the signature of a lead and a melt pond. Due to the limitations of satellite resolution and the requirement for a sufficient number of floe chords within an area, the dataset is limited to floe size with a diameter of 300 m or larger. Additionally, uncertainties are associated with retrieving the mean floe diameter (MFD) in the small floe size range (i.e., MFD $\approx$ 300-1000 m) and in low SIC regions, as the satellite detects a smaller number of freeboards. Unfortunately, this poorly resolved region corresponds precisely to the floe range of the MIZ; therefore, this dataset cannot be used to estimate the MFD within the MIZ directly. However, we hypothesize that we can use it to estimate the FSD-based MIZ (MIZ-FSD) as the region where ice is detected (SIC $\geq$ 15 %) but no floe chords are (MFD $\leq$ 300 m).

While a MIZ-FSD metric is not well constrained by observation, it is generally accepted that the maximum floe size that large swells can break is around 300 m (e.g. Williams et al., 2013; Boutin et al., 2022). Therefore, this MIZ-FSD definition is a lower-bound estimate for the region affected by waves as it represents areas where a significant fraction of the floes are frequently broken, but a weaker or less frequent wave fracture may be present in regions with a larger MFD. In Horvat et al. (2019), an alternative definition for the MIZ is the area where wave-induced fracture occurs at least once in a month (MIZ-frac) (i.e., where the monthly averaged change in FSD to the first floe size category caused by wave-fracture is non-zero, see for example Figs. 5.9 d & 5.11 b). This definition remains applicable only to model output since there is currently no way to measure the wave-induced fracture occurrence from satellite data.

Coincidentally, this threshold is also used as the default floe size for the lateral melt parameterization within CICE when the FSD option is deactivated. This also represents a physical threshold where the floe perimeter is highly sensitive to a change in floe size (see Fig. A.1). Therefore, the simulated MIZ-FSD in the model is the region where intensified lateral melt caused by wave breaking can potentially occur.

4.3 Floe-size : ice charts (CIS)

We use the gridded weekly ice chart, available for the 1990-2023 time period from the Canadian Ice Service (CIS) (ECCC, 2022). These charts, delineated by polygons with similar sea ice properties, are created by the visual interpretation of ice specialists using satellite images from RadarSat's synthetic aperture radars (SAR). The dataset covers the Canadian Coast, including the Eastern/Western Canadian Arctic Archipelago, the Hudson Bay, the East Coast of Canada/Saint-Laurence Estuary, and the Great Lakes. The raw data are available in a SIGRID-3 shapefile format and are interpolated onto a 10 km x 10 km EASE grid for comparison with the model gridded data. The ice charts include partial concentration, stage of development (i.e., thickness), and form (i.e., floe size) for three sea-ice categories: thickest ice, second thickest ice, and third thickest ice. Each field is assigned a code representing a qualitative interval for each ice category. We calculate the mean floe size by taking the median value of the floe-size interval, weighted by its partial sea-ice concentration for each ice category using the following convention: ice cake/brash ice/pancake ice (< 20 m), small floes (20-100m), medium floes (100-500m), big floes (500-2000m), vast floes (2-10km), and giant floes (> 10 km). Based on these definitions, we define the MIZ-FSD as areas predominantly populated by medium or small floes and ice-(pan)cake. While these data are primarily qualitative, they provide information regarding the composition of the MIZ. For instance, if the mean floe diameter in a region is smaller than 300 m, most of the area is covered by medium floes or smaller, created by wave-induced fracture.

Chapter 5

Results

We first compare the pan-Arctic CryoSat-2-derived mean floe diameter (MFD) with the gridded CIS analysis of the Radarsat-derived MFD in the Labrador Sea and Baffin Bay region, where both CryoSat-2 and CIS data are available (see thick black line in the figure 5.1).

5.1 CryoSat-2 and CIS-derived floe size

The MIZ-SIC and MIZ-FSD define areas where the thermodynamic and dynamic regime differs from the interior pack ice. In low ice concentration regions (MIZ-SIC), the ice drifts freely, and wave attenuation is low, whereas in regions populated with small floes (FSD-MIZ), the thermodynamic melt and wave attenuation are important. Four possible SIC/FSD regimes exist as discussed below: low SIC/small MFD (SIC ≤ 0.8 and MFD $\leq$ 300 m or undetected), low SIC/large MFD (SIC ≤ 0.8 and MFD > 300 m), high SIC/small MFD (SIC >0.8 and MFD ≤ 300 m or undetected) and high SIC/large MFD (SIC > 0.8 and MFD > 300 m).

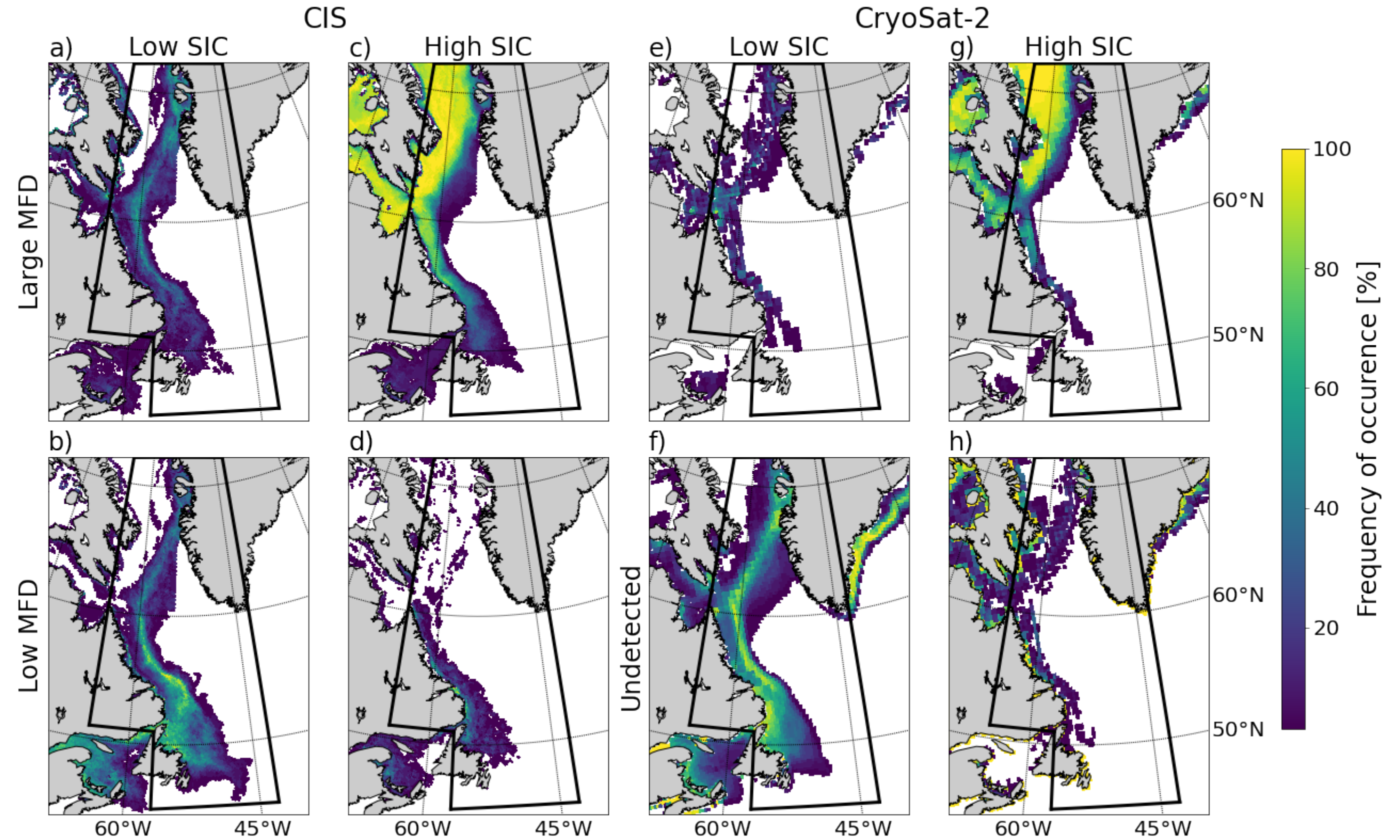

Figure 5.1: Heat map (frequency of occurrence) of the CIS-derived (a,b,c,d) and CryoSat-2-derived (e,f,g,h) four SIC/FSD regimes for the 2010-2018 winters (Jan-Feb-Mar-Apr).

The dominant regimes in the Labrador Sea and Baffin Bay are large MFD in high SIC and small MFD in low SIC areas (Figs. 5.1). The first regime (i.e., consolidated pack ice) is dominant in the Baffin Bay, and its frequency decreases southward along the Labrador coast as large floes are fractured by ocean waves and fracture induced by shear, rotation or divergence along the coastline (Fig. 5.1 c,g). The spatial distribution in CryoSat-2 is similar to that of CIS, except for the tongue of large MFD that is less frequent and does not extend as far south. The second regime is confined toward the ice edge and increases in frequency southward from the northern Baffin Bay and eastward (seaward) from the Labrador coast as ocean waves break the larger floes. In CryoSat-2, this regime is broader and more frequent, suggesting that the altimeter has trouble detecting small floes in low

SIC areas (Fig. 5.1 b,f).

The third regime in order of importance (low SIC and large MFD) mainly consists of large floes advected southward by the Labrador current along the inner boundary of the MIZ-SIC. It has the opposite signature to the low-SIC/small MFD regime with a southward decreasing frequency from the Baffin Bay. In CryoSat-2, this regime is less frequent, again pointing at the satellite's inability to detect (even) large floes in low SIC area (Fig. 5.1 a,e). The last regime (small floes in high SIC) is mainly present along the Labrador coast at the edge of the landfast ice where floe rotation induces fracture and at the mouth of the Groswater Bay, presumably related to local ice formation in coastal polynyas (Fig. 5.1 d). Conversely, the occurrence frequency of this regime (estimated as the residual, where SIC > 0.8) is overestimated in CryoSat-2 with a consistent non-detection of floes along the coastline of the Baffin Island, Greenland, and the Labrador during the 2010-2018 period (Fig. 5.1 h).

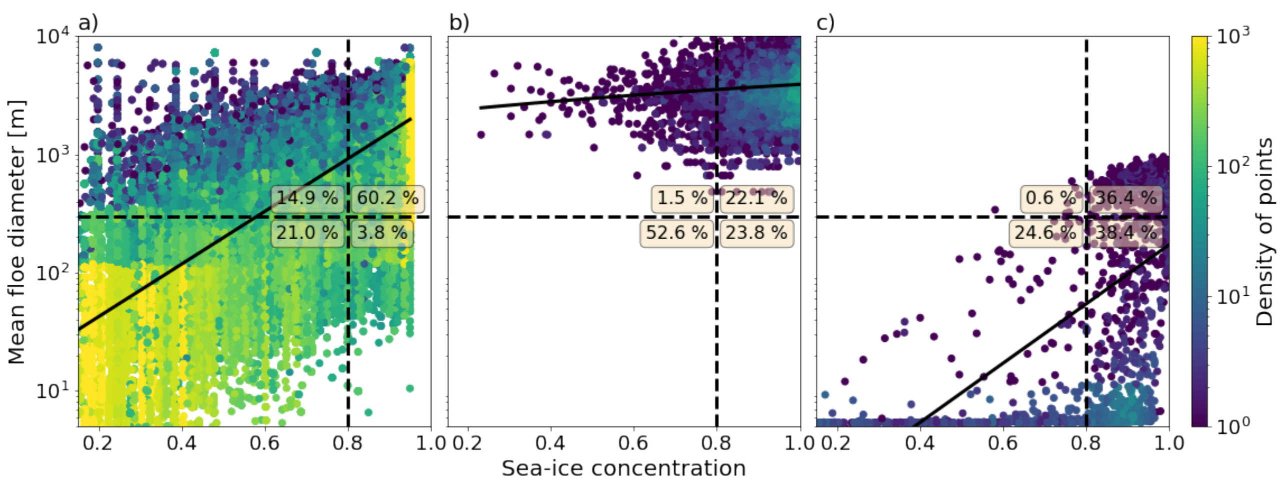

Figure 5.2: Scatter plot of CIS-derived (a), CryoSat-2-derived (b), and simulated (c) SIC and MFD in the Labrador Sea for the 2010-2018 (observations) and 2018 (simulated) winters (Jan-Feb-Mar-Apr). Percentages indicate the fraction of points in each of the four quadrants defined as SIC ≤ 0.8 (MIZ-SIC) and MFD ≤ 300 m (MIZ-FSD). The solid black line represents the best linear fit in a log(y)-x space with (a) $R^2 = 0.57$, (b) $R^2 = 0.02$, and (c) $R^2 = 0.35$.

While the MIZ-SIC and MIZ-FSD definitions are typically considered independently of each other, the correlation ($R^2 = 0.57$) suggests that the MFD generally increases with SIC, representing a gradient of floe size as we move toward the more concentrated inner pack ice (Fig. 5.2 a). Small floes are generally located near the outer ice edge, where high-frequency waves break larger floes into small pieces. Inward the ice edge, the wavelength increase as shorter wavelengths are attenuated preferentially, gradually increasing the floe size. Deeper still in the pack ice, sea ice floes follow the long wavelength of the ocean surface without fracture, leading to a sharp increase in MFD. This relationship suggests that a universal MIZ definition - representative of the region where both thermodynamical and dynamical regimes are different from the inner pack - exists with a higher MFD cut-off or lower SIC cut-off (e.g., SIC $\leq$ 0.6 or MFD ≤ 1000 m, Fig. 5.2). In CryoSat-2, no correlation exists between the MFD and the SIC (i.e., $R^2 = 0.02$) again because large/small floes are mostly undetected in low SIC areas.

In CIS ice charts, the MIZ-SIC covers a smaller fraction of the Labrador domain over the 2010-2018 period (i.e., two left quadrants in Fig. 5.2 a) compared with MIZ-SIC extent derived from NSIDC-CDR SIC. This overestimation of the MIZ-SIC in CryoSat-2 mostly comes from the position of the 0.8 concentration contours that is further within the pack ice in the NSIDC-CDR dataset instead of the position of the ice edge (Figs. 5.3 & 5.4). Whether the different resolution of the datasets causes such discrepancies, the qualitative nature of the CIS data, or biases in the sea-ice concentration retrieval from passive microwave measurement needs to be clarified.

Similarly, MIZ-FSD areas are also overestimated in CryoSat-2 (Figs. 5.2 a,b). The most significant contributor to CryoSat-2's MIZ-FSD overestimation comes from the non-detection of both small and large floes in low SIC regions (Fig. 5.4) but is further amplified by the large residual in high concentration (small MFD, large SIC) that were rare in CIS analysis. Note that the CryoSat-2's MIZ-SIC and MIZ-FSD extent both depends on

NSIDC-CDR SIC biases; the former directly because of the positions of the 0.15 or the 0.8 concentration contours, and the latter indirectly because of the poor detection in those low concentration regions.

The comparative analysis of CryoSat-2-derived and Radarsat-derived MFD suggests that in CryoSat-2 data, out of the total undetected floes in the MIZ-SIC, only a fraction remain undetected due to their floe size falling within the MIZ-FSD range. CryoSat-2-derived MIZ-FSD (defined as the area within the SIC = 0.15 contour and the absence of floe chords detected by the satellite) overestimates the "true" MIZ-FSD because of the lack of freeboard measurements in the 300-1000m range, in low-concentrated regions, and along the coastline. In the following, considering the biases discussed above, we assess the realism of the simulated MIZ-FSD/SIC from CIS/CryoSat-2 observations in the Labrador region first, then to CryoSat-2 observations in the pan-Arctic.

5.2 Simulated and observed MIZ

5.2.1 Labrador/Baffin Bay

The seasonal cycle of the MIZ-SIC and MIZ-FSD generally agrees with observations, although significant positive and negative biases are present in the winter MIZ-FSD and MIZ-SIC extent, respectively. In contrast with observations where the MIZ-SIC is larger than the MIZ-FSD in winter, the simulated small floe size area extends far beyond the 0.8 concentration contour, indicating wave-induced flexural failure deep within the consolidated ice cover (Figs. 5.3 & 5.4). For instance, in March, the simulated MIZ-FSD is much more extensive in the northern Baffin Bay (red contours in Fig. 5.4 c), compared with observation where the MIZ-FSD follows closely the MIZ-SIC (Figs. 5.3 & 5.4 a,b). The presence of larger floes in the Baffin Bay is represented in the model, but the southward advection of those large floes (MFD ≈ 1 km) along the Labrador coast is not, as the wave-induced floe fracture affects the entire width of the ice tongue advected by Labrador current (Fig. 5.4).

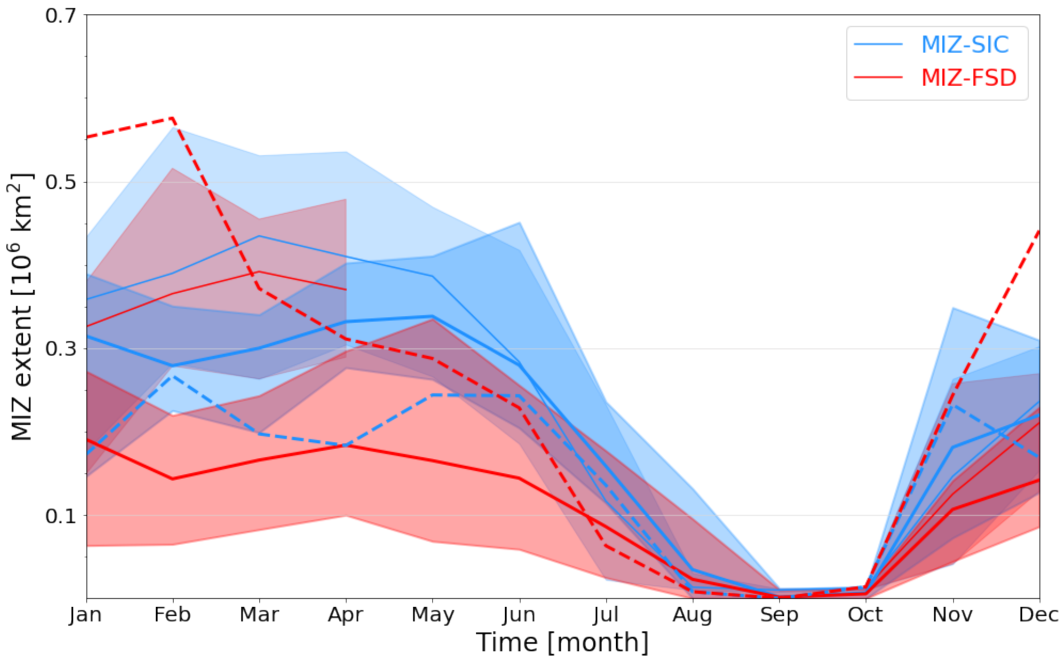

Figure 5.3: Seasonal cycle of the simulated (dashed), CryoSat-2 (thin solid) and CIS (thick solid) mean MIZ-SIC ($0.15 \leq$ SIC ≤ 0.8) (blue) and MIZ-FSD (MFD $\leq$300 m) (red) extent in the Labrador Sea for the 2010-2018 (observation) and 2018 (simulated) periods, respectively. The shaded area represents the minimum and maximum values from the 8-year observational period. High SIC/small MFD regions are not considered in both observational datasets.

Conversely, the model displays the narrowest MIZ-SIC extent, followed by ice charts and satellite-derived MIZ-SIC respectively (Figs. 5.3 & 5.4). From this low-concentration region, occurrences of large floes in low sea-ice concentration areas in the model are rare (Fig. 5.2 c). Instead, most grid points in the MIZ-SIC have a constant small floe size ($\approx$ 5 m, the smallest floe-size category), indicating that wave-induced redistribution of areal FSD is mostly from large directly to the smallest floe category. In addition, small floes occupy a significant fraction of the pack ice (SIC $>$ 0.8) (see the lower-right quadrant in Fig. 5.2 c). The presence of small floes in high SIC areas leads to a lower correlation between the SIC and MFD in semilog space ($R^2 = 0.35$) as wave-fracture fails to redistribute floes in the larger category with the increase of concentration and the gradual damping of short wavelengths.

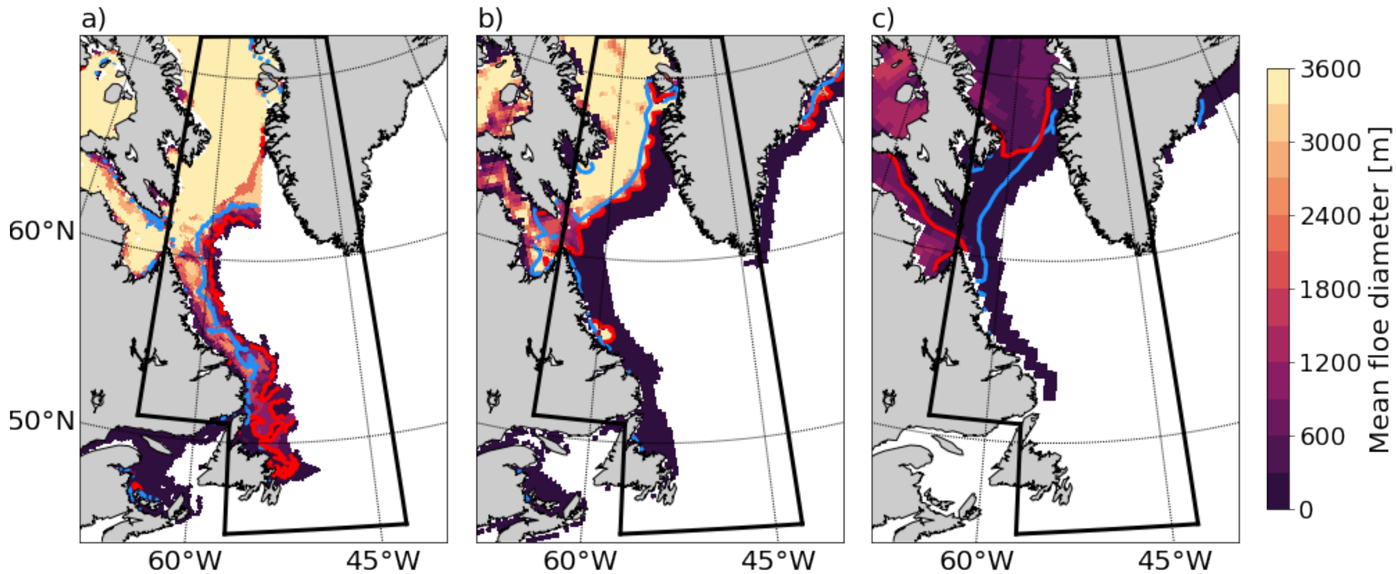

Figure 5.4: CIS-derived (a), CryoSat-2-derived (b), and simulated (c) mean floe diameter in the Labrador Sea region for March 2018. Blue and red lines represent the MIZ-SIC and the MIZ-FSD edges, respectively. Satellite-derived sea-ice concentration comes from the NSIDC-CDR dataset in b). Only data where SIC is higher than 15 % are shown.

5.2.2 Pan-Arctic

At the pan-Arctic scale, the model captures the seasonality but underestimates MIZ-SIC extent by a factor of 2 compared to satellite-derived SIC, mainly due to the sharper transition from the open water to the compact pack ice and an underestimation of the southern extent of the ice edge (Figs. 5.5 & 5.6). This feature is especially marked in the Labrador region and could be related to the strong observed ice-edge signature in the atmospheric forcing, the low resolution of the model, or the use of the slab ocean forcing.

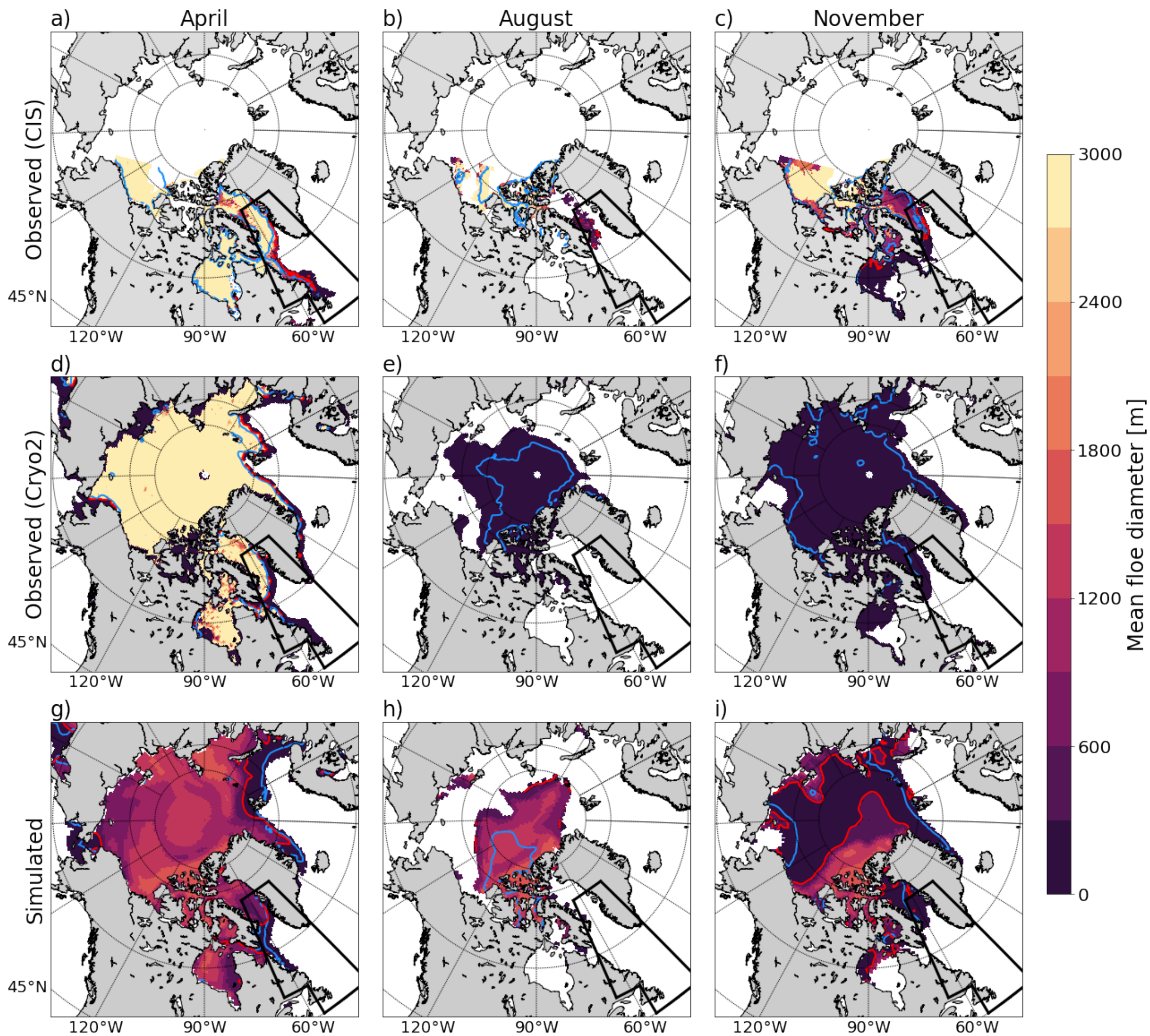

Figure 5.5: CIS-derived (a-c), CryoSat-2-derived (d-f), and simulated(g-j) mean floe diameter in April, August, and November. Blue and red lines represent the MIZ-SIC and the MIZ-FSD edges, respectively. Satellite-derived sea-ice concentration comes from the NSIDC-CDR dataset in (d-f). Only data where SIC is higher than 15 % are shown.

The simulated seasonality of the MIZ-FSD extent is largely overestimated, with values three times larger than observation in fall and winter. In November, it reaches ≈ 6 million km^2, which occupies nearly the entire Arctic Basin, and reach only ≈ 0.5 million km^2 in August (Fig. 5.6 a). In summer (Jun to Aug), the simulated MIZ-FSD in the control run is much narrower than the MIZ-SIC due to the absence of large waves (weaker winds in summer) combined with the melt of the smaller floes (MFD $\leq$ 300 m). The increase in SIC-MIZ in summer is associated with an increase in MIZ-frac area, as waves can propagate farther in the looser ice cover. However, such an increase in MIZ-frac does not translate into an increase in MIZ-FSD: waves are too small to significantly alter the floe size, suggesting that wave fracture does not play a dominant effect in summer (Fig. 5.6). Whether the simulated mean floe size and pan-Arctic MIZ-FSD are realistic in the melting season cannot be assessed as any pan-Arctic observations are available. The presence of small floes in the Beaufort Sea reported in (e.g. Manucharyan et al., 2022), which are also observed in the CIS data (e.g., Fig. 5.5 h) suggest that the model underestimate the MIZ-FSD in summer and that thermodynamic processes are also being responsible for the disintegration of the pack ice into smaller floes in summer.

In fall, the MIZ-FSD is much wider than the MIZ-SIC when storm activity returns, causing waves-induced fracture deep into the loose pack ice, in contrast with CryoSat-2 derived MIZ-FSD where the wave-induced fracture is limited to the MIZ-SIC region (Figs. 5.5 & 5.6). While the MIZ-FSD criterion applied to satellite-derived MFD overestimate MIZ-FSD extent in the Labrador/Baffin Bay region, such overestimation does not alter the conclusion that biases exist in the model as in reality, the CryoSat-2-derived MIZ-FSD extent should be even smaller.

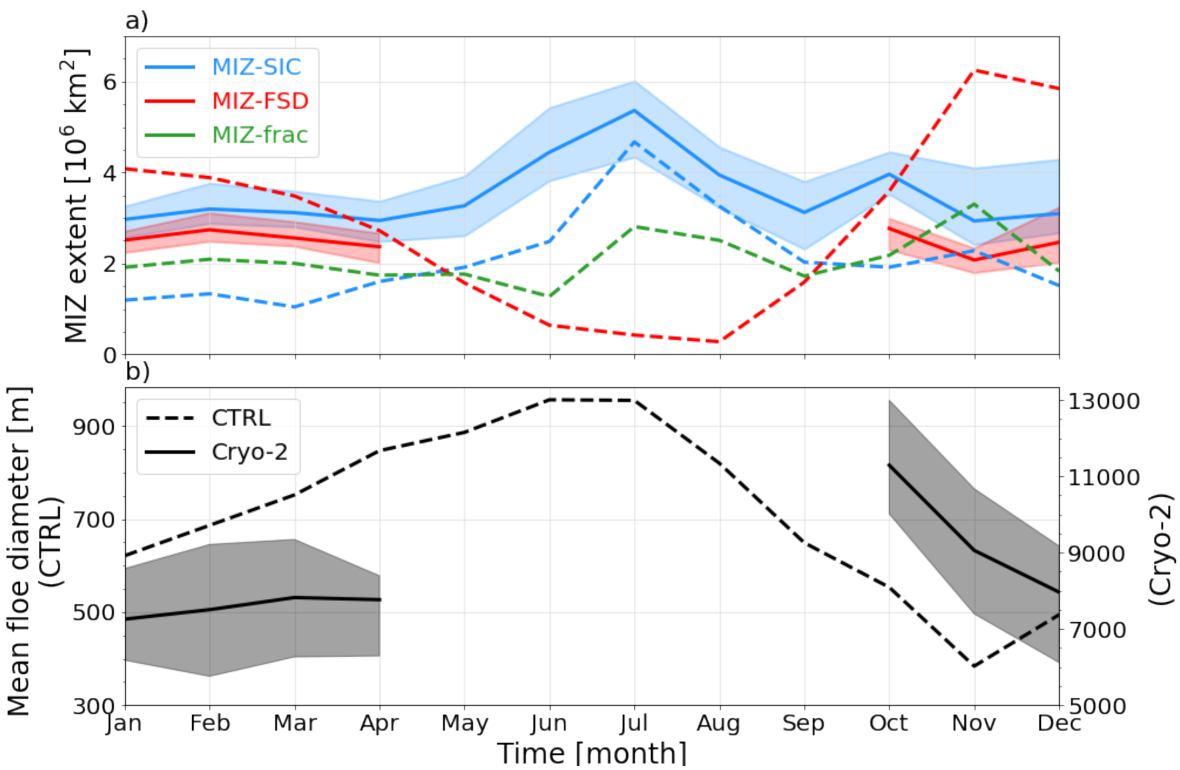

Figure 5.6: Pan-Arctic seasonal cycle of observed (solid) and simulated (dashed) (a) MIZ-SIC (blue), MIZ-FSD (red) extent, and (b) average mean floe diameter for the 2010-2018 (observation) and 2018 (simulated) periods. The green dashed line in (a) is the region where wave-induced fracture occurred at least once a month in the model (frac-MIZ). The shaded area represents the min and max from the 8-year observational period. High SIC/small MFD regions are not considered in the CryoSat-2 dataset.

We note that the simulated mean floe size within the pack is an order of magnitude smaller when compared to observation (Figs. 5.6 b and 5.5). This is because the AI-based fracture model only considers ocean wave-related fracture processes (with 12 FSD categories between 0 and 1 km) and ignores dynamic fracturing that results in floes with diameters ranging between 1 and 10 km (Roach et al., 2018, 2019). Also, the observed decrease in CryoSat-2 derived MFD in fall does not appear to be related to wave fractures, as this decrease is not associated with an increase in MIZ-FSD. We hypothesize that it results from the lack of small floes detection when the SIC is low (Fig. 5.2), leading to a larger floe size where measurements are available.

Lastly, in winter, the MIZ-FSD is higher than the MIZ-frac - meaning that small floes exist even where wave fracture did not occur - and both are higher than the MIZ-SIC - meaning that wave fracture occurs deep within the pack ice, which does not appear to be supported by observations (Fig. 5.5). Those discrepancies between these MIZ definitions suggest three possibilities: 1) the wave attenuation is too weak, allowing for the propagation of waves that break the ice deep into the consolidated ice cover, 2) the fracture scheme expressed as a function of wavelength and height is too sensitive, and 3) other floe size processes are not tuned correctly (e.g., new-ice formation, welding). Going further into the last key point, the spatial pattern of MIZ-FSD is correlated with the area where wave fracture occurred in the previous months, suggesting that absence of regrowth may also be at fault in the fall/early winter.

5.3 Model sensitivity to wave attenuation

In the winter, the FSD is governed by wave-dependent ice fracture and new ice formation and growth processes. Wave fracture promotes small floes generation depending on the wavelength and height and decreases in importance from the ice edge. In turn, new ice formation promotes large floes generation only in calm (no waves) conditions as it depends on the tensile failure limits and, therefore, increases in importance from the ice edge. As a result, a change in the wave attenuation schemes affects the wave energy spectrum, which in turn affects both wave fracture and ice formation leading to a complex response and different FSD and MIZ-FSD extent (Fig. 5.7).

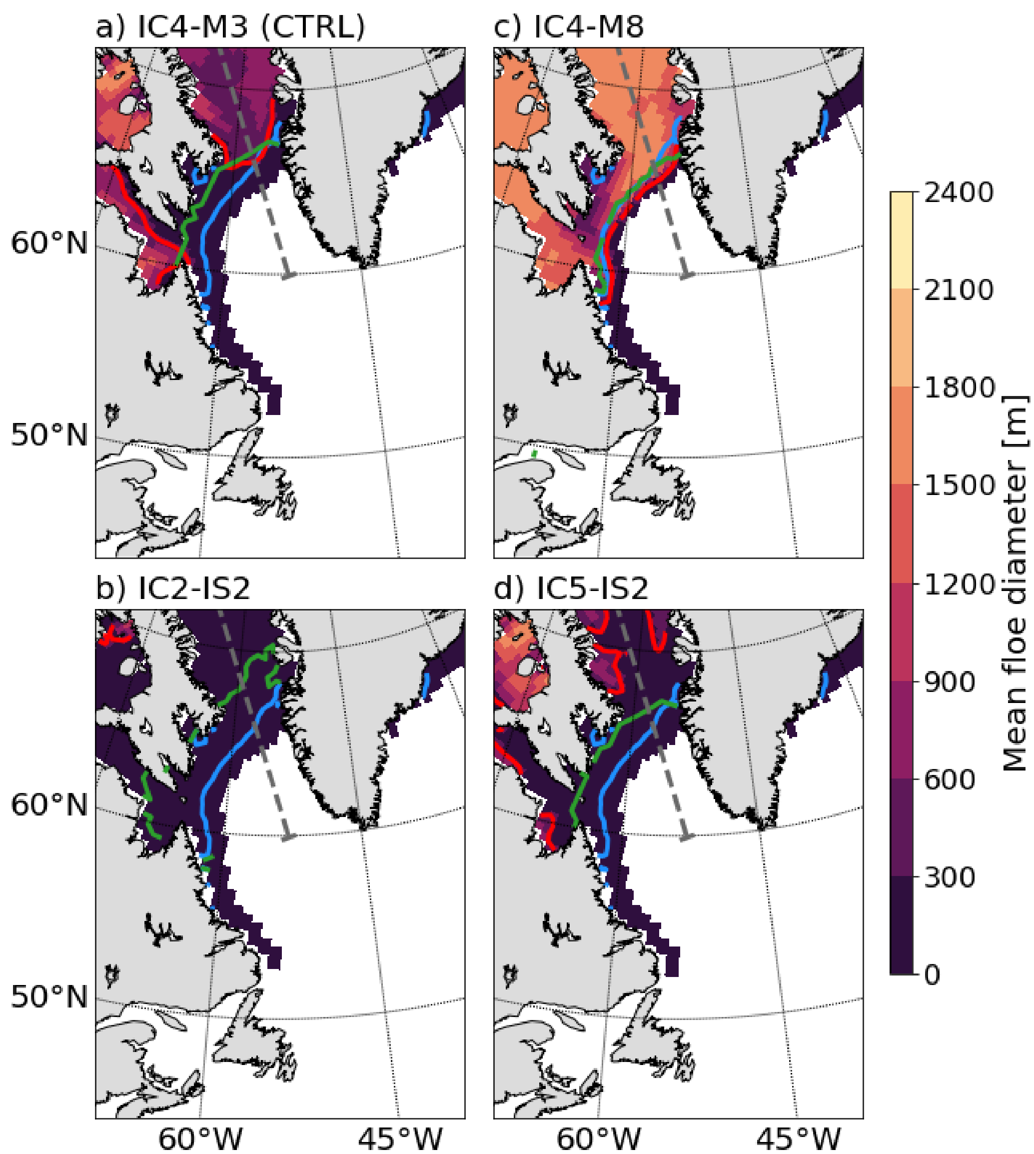

Figure 5.7: March simulated mean floe diameter in the Labrador Sea region for different empirical (a), (c) and theory-based (b), (d) attenuation schemes (thin elastic (b) and viscoelastic layer respectively (d)). Blue, red, and green lines represent the edge of the MIZ-SIC, the MIZ-FSD, and the MIZ-frac, respectively. Only data where SIC is higher than 15 % are shown. The dashed gray line indicates the cross-section in Fig. 5.8.

The choice of wave attenuation formulation has a negligible effect on the MIZ-SIC extent in winter suggesting that the MIZ-SIC is mostly governed by ocean heat flux and air-sea interactions. The MIZ-FSD (and MFD), on the other hand, is highly sensitive to the wave attenuation scheme (Fig. 5.7). Empirical formulations (Fig. 5.7 a,c) lead to a narrower MIZ-FSD compared to the theory-based one, where small floes populate the entire Labrador Sea/Baffin Bay as well as the whole Arctic (figure not shown) (Fig. 5.7 b,d). The floe-dependent empirical attenuation scheme (IC4-M8) displays the most realistic MIZ-FSD extent: the MIZ-FSD is confined to the low-concentrated region, a key feature reported in observation but that is not simulated in the control run.

The reason for the differences in MIZ-FSD extent is most apparent in the wave spectrum and significant wave height (H_s) evolution along a transect perpendicular to the ice edge (Fig. 5.8 a). The empirical floe-dependent parameterization (IC4-M8) has the stronger attenuation with a marked decline in short wavelengths by smaller floes present before the ice edge (SIC < 0.15) (Fig. 5.8 c). This lack of floe size dependency in the control-run lead to a slower attenuation in the first hundreds of kilometers, but eventually, the two schemes reach similar values deep into thicker and more consolidated pack ice (Fig. 5.8 a). While theory-based formulation (IC2-IS2 and IC5-IS2) also includes a floe size dependency (via scattering and creep-based dissipation), the preferential attenuation of short wavelength is much smaller than what is simulated by the floe-dependent empirical scheme (IC4-M8).

When waves reach the 0.8 concentration contour (i.e., roughly 180 km from the ice edge), the wave height in the most dissipative scheme (IC4-M8) is an order of magnitude lower than the waves in the least dissipative one (IC2-IS2) (Fig. 5.8 a). Short wavelengths are more attenuated in the viscoelastic model (IC5-IS2) than in the other theory-based scheme based on the thin plate theory (IC2-IS2) (Fig. 5.8 d). Empirical formulations effectively act like a low-pass filter, mainly removing wavelengths below ≈ 100 m for the IC4-M8 and ≈ 75 m for the IC4-M3. The mid-range attenuation is strongest for the IC4-M8, followed by the IC4-M3, the IC5-IS2, and the weakest attenuation for the IC2-IS2, but all the parameterizations produce similar damping in the longwave range. Deep into the pack ice, the results are similar (Fig. 5.8 e), except for the thin-elastic plate formulation showing a much more energetic spectrum, particularly in the short-wave range. As a result, the associated significant wave height reach 10 cm, even at a 700 km distance from the ice edge, compared to roughly 1 mm and 1 cm in the empirical and the viscoelastic formulation, respectively (Fig. 5.8 a).

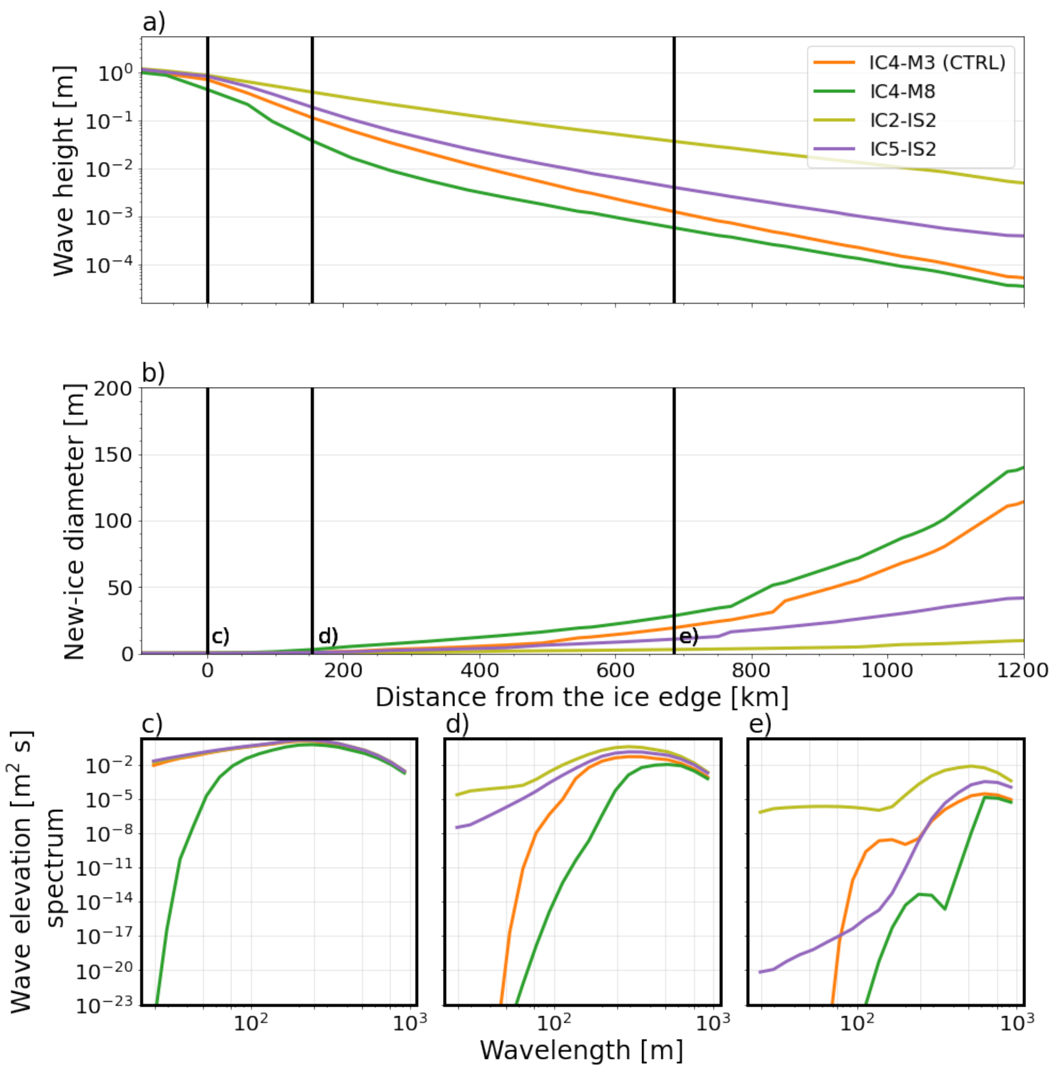

Figure 5.8: Sensitivity of the spatial variation of the significant wave height (a) and new-ice diameter (b) as a function of the distance from the ice edge along a cross-section in the Baffin Bay (see the gray dashed line in Fig. 5.7) in the simulations for empirical (green, orange) and theory-based (yellow, purple) attenuation scheme. Wave elevation spectrums are shown along the transect at the ice edge (c), the inner boundary of the MIZ ($SIC = 0.8$) (d), and deep into the pack ice (e).

The reason why a more dissipative scheme appears to be an essential requirement for the model to reproduce a realistic mean floe size and MIZ-FSD extent is two-folded: 1) it reduces the distance from the ice edge where the wave-induced fracture occurs (Fig. 5.7), and 2) it increases the floe size category at which the new-ice can be added in the pack (Fig. 5.8 b).

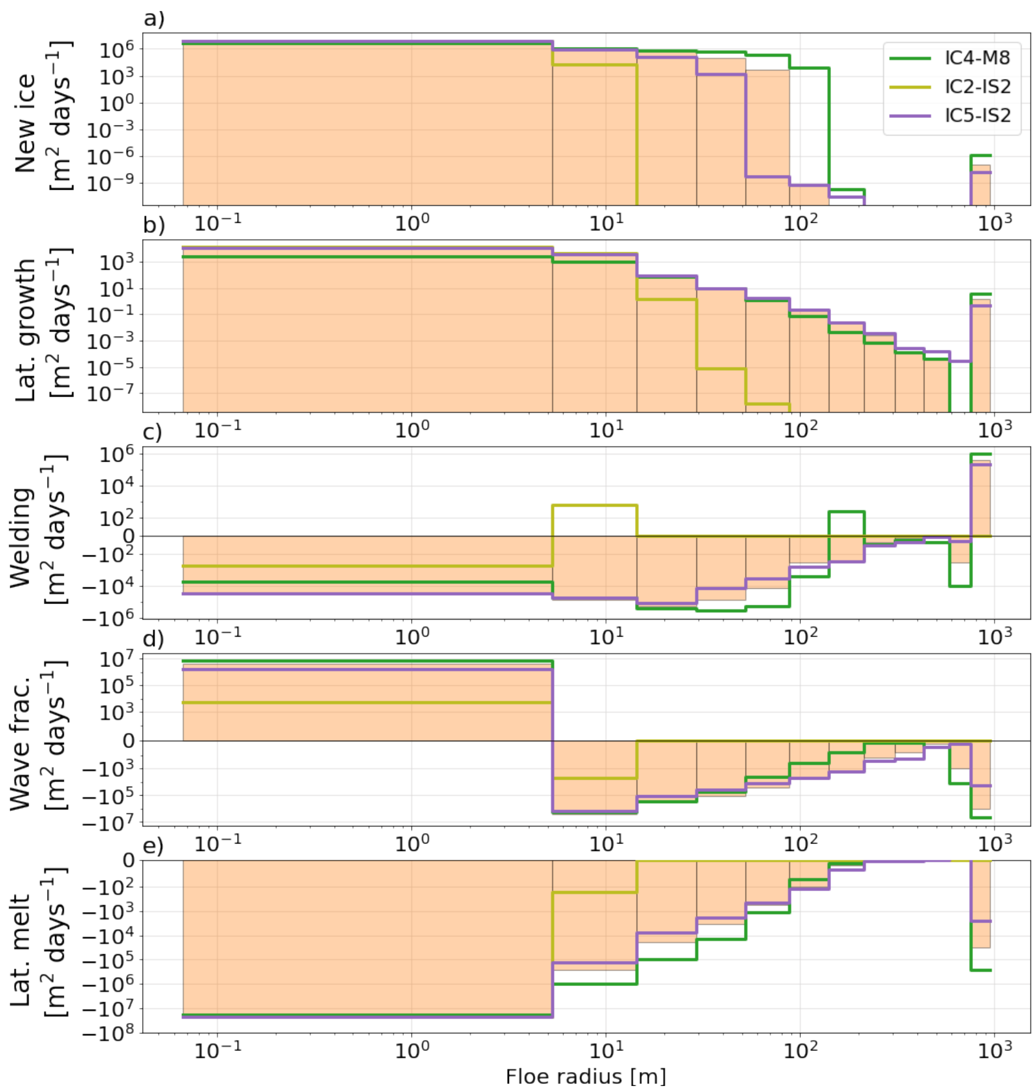

Figure 5.9: Average change in ice area in each floe size category (a) new-ice formation (b) lateral growth (c) welding (d) wave fracture (e) lateral melt in the sensitivity simulations for empirical (green, orange) and theory-based (yellow, purple) attenuation schemes over the Labrador/Baffin Bay domain for March.

First, the choice of the attenuation scheme influences the penetration of wave fractures within the pack ice as depicted by the MIZ-frac (green line in Fig. 5.7). Due to their stronger wave dissipation, empirical attenuation schemes result in narrower MIZ-frac than theory-based formulations. However, regardless of the attenuation formulation, the wave fracture scheme redistributes the ice toward the smallest floe size categories, even using the IC4-M8 attenuation scheme, where shorter wavelengths are mostly filtered (Fig. 5.9 d). In observations, the correlation between the SIC and the FSD (seen in Fig. 5.2 a) shows an increase of the MFD with SIC as the ice attenuates short wavelengths preferentially. This highlights one of the flaws of using a strain-based wave fracture parameterization - recall that the superparameterization requires the identification of triplets of extremum in a reconstruction of the sea surface height (see chapter 3.1). By assuming that ice floes are following perfectly the wave field, the presence of the short wavelengths in the wave spectrum reduces the distance between consecutive extremums, which results in fracture histograms mainly composed of the smallest floe size category. Also, we note that wave fracture is omnipresent where a significant wave height larger than 0.1 m is simulated in winter (corresponding to an arbitrary threshold fixed to reduce the false positive rate by the machine learning fracture model). Therefore, instead of producing a smooth gradient of floe size in the MIZ as in the CIS ice charts, the machine learning fracture scheme trained on the strain-based physical model systematically breaks all the ice towards the smallest category with minor sensitivity to the wave height or wavelength.

Second, from three contributions that can lead to an increase in floe size in the FSD equation (i.e., new-ice formation, welding, and lateral growth), welding and lateral growth are typically orders of magnitude smaller than the new-ice formation (Fig. 5.9 a,b,c). The new-ice formation consists in a very efficient way to create large floes but requires the presence of long wavelengths and a highly attenuated wave field. New ice is mostly always added to the first or second floe size category for the thin-elastic plate theory attenuation scheme (IC2-IS2), while a more dissipative scheme (like the IC4-M8) allows for the formation of larger floes in the pack ice (Figs. 5.7 b & 5.9). The presence of floes in larger categories further stimulate the generation of larger floes via welding. With the IC2-IS2 attenuation scheme, welding transfer ice from the first to the second category, but then wave fracture redistribute an equivalent amount toward the smallest floe category, deactivating any ice growth (Fig. 5.9 c). Using the IC4-M8 formulation, a larger fraction of the ice moves toward the last floe size category compared to the other attenuation schemes, which results in the growth of the floes and the largest MFD in the pack ice. Therefore, the new-ice formation also partly explains why the simulated region of small floes (MIZ-FSD) is so broad with some of the attenuation schemes, as the MIZ-FSD does not only include areas where wave fracture occurred (see the region of small floes simulated outside of the MIZ-frac in Fig. 5.7) but also where the presence of a wave field turns off the regrowth of large floes.

5.4 Dynamic and thermodynamic effect of the coupling

For this last section of the result, we focus on the effect of the wave-ice interaction on the sea-ice area along the Baffin Bay and Labrador coastline, where significant biases in SIC attributed to rapid ice deterioration events were identified (Browne et al., 2017). Waves can change sea ice conditions directly because of the transfer of momentum from the wave field to the ice (dynamic) and or indirectly via an increase in the floe perimeter (thermodynamic), and both contributions have competing effects (Figs. 5.10 & 5.12).

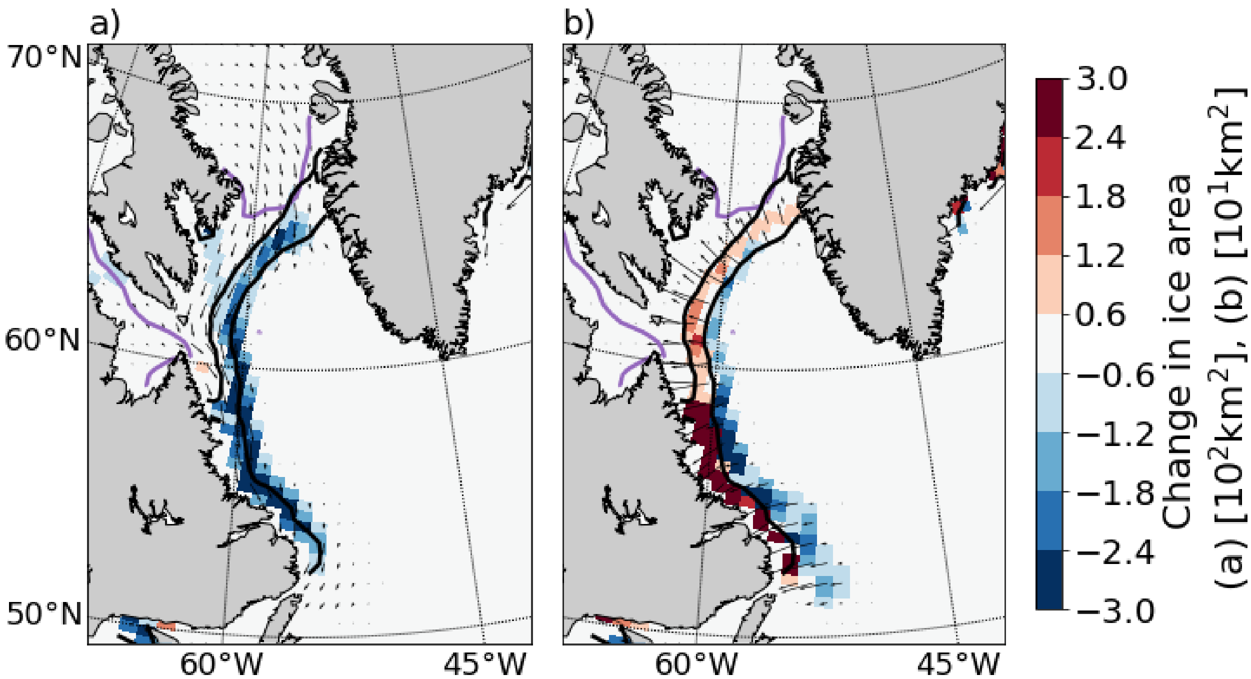

Figure 5.10: March 2018 ice area anomalies between the (a) control and the non-coupled run (b) control and without WRS run. Blacks and purple lines represent the edge of the MIZ-SIC and the MIZ-FSD, respectively. Arrows show the ice velocity (a) and the wave radiation stress (b).

We quantify the thermodynamical effect of the coupling by taking the difference between the simulation with and without FSTD (Fig. 5.10 a). When the FSTD is deactivated, the lateral melt is parameterized by the same formulation of Steele (1992), but the effective diameter for melting is set to a constant (300 m). In the coupled model, incoming waves break the ice cover in small pieces, which leads to a decrease in average diameter (lower than 300 m) and increase lateral melt, resulting in negative concentration anomalies (Fig. 5.4). March anomalies in the sea ice area are mostly contained within the MIZ-SIC: the loose sea ice cover allows for more surface contact with the ocean, and the ice encounters warmer water, increasing the melting potential. Therefore, even if small floes are observed deeper in the pack (see purple contour), anomalies are much weaker in those regions. The negative concentration anomalies are spatially correlated with the lateral melt, but the wave breaking is the largest at the inner edge of the MIZ-SIC where large floes are advected (Figs. 5.10 a & 5.11 a,b).

Similarly, we quantify the dynamical effect of the coupling by taking the difference between the simulation with and without WRS (Fig. 5.10 b). The anomalies are primarily contained in the MIZ-SIC, where waves are strongly attenuated, leading to a strong momentum transfer. Outside this region, the horizontal gradient of energy loss is much weaker, and the WRS is negligible (Fig. 5.11 c). In the MIZ-SIC, the sea-ice area anomalies are positive, while the anomalies outer edge MIZ are negative, displaying a dipole pattern. This indicates a convergent motion, with waves pushing sea ice toward the inner SIC-MIZ amplified by the presence of a coastline. The same dipole anomaly would be observed without a coastline because of the internal ice stress that increases from the sea ice edge to the pack ice's interior as the SIC increases. The dynamic anomalies are spatially correlated with the normalized stress (a measure of the relative importance of the wave radiation stress and surface wind stress) (Figs. 5.10 b &. 5.11 c).

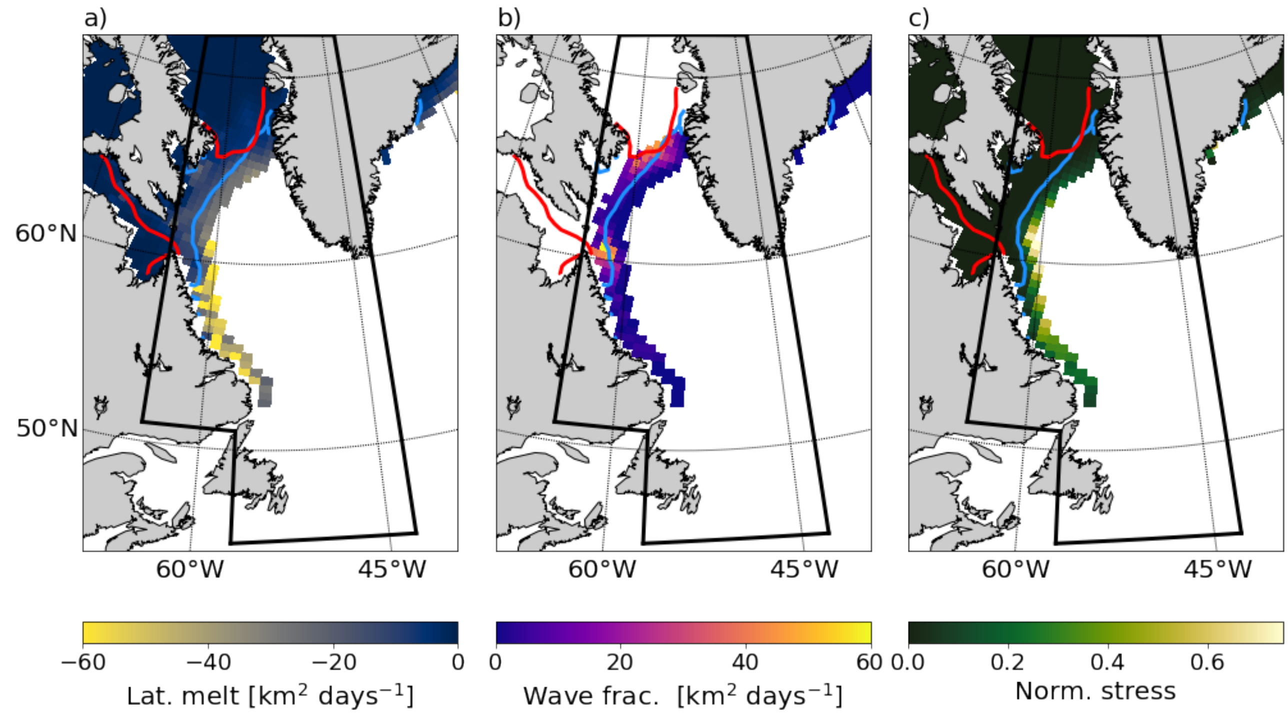

Figure 5.11: March 2018 change in ice area from (a) the total lateral melt, (b) in the first floe size category generated by wave fracture, and (c) the normalized stress ($\frac{\tau_{wave}}{\tau_{wave}+\tau_{air}}$). Blue and red lines represent the MIZ-SIC and the MIZ-FSD edges, respectively.

Results are consistent throughout the winter with negative concentration anomalies between the fully coupled and the no FSTD simulation in the MIZ-SIC in the Labrador/Baffin Bay region. The average anomalies peak in summer, reaching $\approx$ -300 km^2 in June when warm water melts small floes (Fig. 5.12). The dynamic effect is almost always weaker than the thermodynamic effect, with absolute anomalies reaching $\approx$ 50 km^2 in June when the sea ice is more mobile. These results suggest that the WRS is not playing a significant role in the width of the MIZ and that the dynamic effect remains primarily compensated by the thermodynamics. At the daily time scale, the effect of the WRS is even more negligible compared to thermodynamic contributions (not shown).

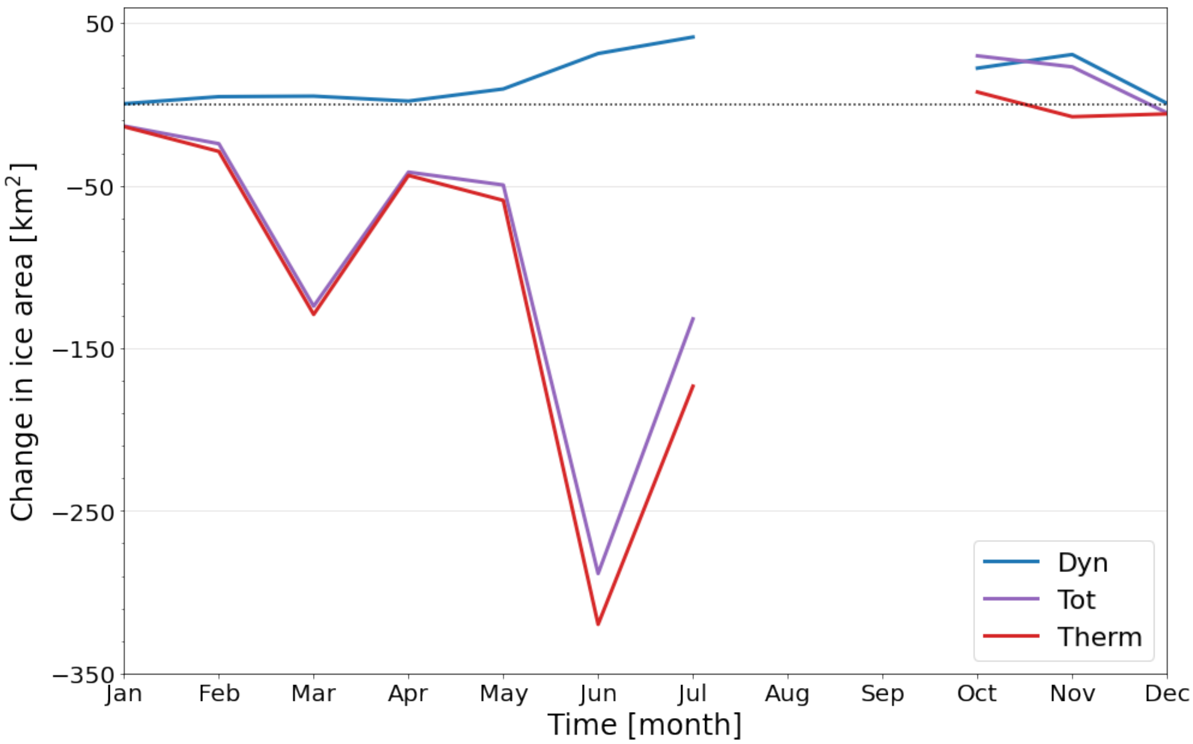

Figure 5.12: Evolution of the monthly dynamic, thermodynamic, and total sea ice area anomalies in the MIZ-SIC over the Baffin Bay/Labrador domain in 2018.

We hypothesized that the hourly coupling set-up would allow for a representation of wave-ice feedback where an intense lateral melt due to an increase in the perimeter occurs after wave fracture and causes rapid wave-induced ice deterioration events. However, while the coupled model produces an increased monthly lateral melt, the total melting does not come from discrete, rapid contributions but from a steady contribution throughout the melting season that is uncorrelated with the presence of waves. This is a direct consequence of overestimating the simulated wave fracture and the MIZ-FSD extent in the model since all the floes are consistently broken in the smallest floe size category in the MIZ-SIC, compared to observations where a gradient of MFD that increases with SIC is observed. Therefore, the wave-fracture term is negligible in most of the MIZ-SIC, except at its inner edge, where larger floes are advected. The fracture of those floes does not depend on the presence of large waves as they are systematically fractured no matter the wave field and does not result in a rapid increase in the lateral melt (Fig. 5.11 a,b). In this sense, using such a set-up, an hourly coupling is unnecessary, and the simple presence of a daily or weekly wave forcing would lead to similar results as long as a more realistic FSTD model is not implemented. For this reason, this section is not included in the final manuscript as we consider that further improvement of the coupled model is still required to better represent the small-scale processes at play in rapid breakup events.

Note that the effect of the WRS is more significant in other studies. For example, in Boutin et al. (2020), they found that the WRS effect is stronger than the thermodynamic effect at a daily timescale. They attribute that to cases where the WRS is not oriented toward the ice edge because locally generated waves push ice toward the open ocean, which is not allowed in our model. In Boutin et al. (2021), they use a much higher resolution model, and they link fragmentation to damage, causing fractured ice to be much more mobile, resulting in a much stronger compacting effect of the WRS on SIC. This suggests that using a granular rheology or linking the effect of the damage with wave fracture is critical in representing the compacting effect of the WRS.

Chapter 6

Discussion and conclusion

In this study, we investigate the realism of the simulated floe size distribution (FSD) and marginal ice zone (MIZ) extent using one of the most advanced coupled wave-ice models publicly available: the CICE dynamical core, the Icepack column physic with a joint floe size and thickness distribution (FSTD) and the WAVEWATCHIII (WW3) third generation wave model. To this end, we compare the simulated MIZ extent defined with the sea-ice concentration (SIC) (MIZ-SIC, i.e., $0.15 \leq \text{SIC} \leq 0.8$) and with the mean floe size (MFD) (MIZ-FSD, i.e., MFD $\leq$ 300 m and SIC ≥ 0.15) against passive microwave-derived SIC from the National Snow and Ice Data Center climate data records (NSIDC-CDR), MFD derived from CryoSat-2 floe chords altimetric measurements as well as RADARSAT-derived SIC and MFD from the Canadian Ice Service (CIS).

We first compare the lower-resolution CryoSat-2-derived against the higher-resolution CIS-derived MFD in the Labrador/Baffin Bay region, where both datasets are available. Results show that even if the floe chord detection threshold is 300 m, CryoSat-2 has difficulty detecting MFD in the $\approx$ 300-1000 m floe size range, in low-concentrated and in coastal regions (even if SIC is large). Therefore, using such a MIZ-FSD definition overestimates its extent by considering not only regions where the MFD is below the detection limit but also regions where the lack of floe chord measurements incapacitates the MFD retrieval. We also note differences in the SIC-MIZ extent due to the position of the 0.8 SIC contours penetrating deeper in the NSIDC-CDR dataset compared to RADARSAT-derived SIC from the CIS. We hypothesize that the positive MIZ-SIC extent biases in the Labrador Sea are related to the SIC retrieval from passive microwave measurement but this is left an open question.

Results from a control simulation using a thickness-dependent empirical attenuation scheme (Horvat and Tziperman, 2015; Roach et al., 2018, 2019) show that the model vastly overestimates the region of small floes broken by waves (MIZ-FSD) and underestimates the southern extent of the ice edge, as well as the penetration of the 0.8 concentration contour (SIC-MIZ) in the Labrador/Baffin Bay region. In winter, the model simulates an intense wave fracture, affecting the entire width of the SIC-MIZ and fracturing ice floes into an MFD of $\approx$ 5m in the whole region, while both observational datasets show that unfractured large floes populate a significant fraction of the SIC-MIZ. At the pan-Arctic, the effect is even more substantial, with a MIZ-FSD extent that reaches 6 million km^2 in November, representing almost the totality of the ice cover. In summer, the rapid melt of the small floes combined with a decrease in activity results in an increase of the global MFD and a decrease of the MIZ-FSD extent, but no observations are available for validation. The simulated seasonal cycle of the MFD and MIZ-FSD are consistent with what is reported in other studies using similar model configurations (Roach et al., 2019; Cooper et al., 2022). Here, we reappraise the realism of such a spatial and temporal MFD pattern in winter: We show that in observation, the wave-induced fracture is confined to low-concentration regions, a crucial feature that the model does not systematically reproduce. Three possibilities are investigated to explain this overestimation of the MIZ-FSD: 1) the wave in ice attenuation is too weak, 2) the wave fracture model is too sensitive, and 3) the regrowth of floes is too slow.

To this end, we test the sensitivity of the model to a range of wave attenuation schemes (see table 3.1), including another empirical scheme, but with a floe size dependency (IC4-M8) and two theory-based formulations based on a thin-elastic plate (IC2-IS2) and a viscoelastic layer model (IC5-IS2). Results show that the most dissipative scheme (IC4-M8) leads to the most realistic MFD and FSD-MIZ extent by reducing wave-induced fractures and increasing large floe formation deep within the pack ice.

However, note that uncertainties remain concerning the wave attenuation schemes. Empirical attenuation schemes are to be used cautiously at a global scale, as local measurements in the MIZ do not necessarily apply to all types, floe sizes, or thicknesses of ice. Theory-based formulations like the one developed in Boutin et al. (2018) result in an unrealistic wave penetration even in the most consolidated ice cover. This configuration is validated to satellite measurements in the recent study of Boutin et al. (2022), suggesting that the wave attenuation is realistic near the ice edge. However, the resolution of the satellite does not allow for wave validation deeper in the pack (wave height less than 0.5 m) and does not distinguish between locally generated waves and waves propagating through the ice cover from the open ocean. Also, increasing the horizontal resolution to represent small-scale heterogeneity in the ice cover could lead to a different attenuation.

We stress, however, that the wave attenuation scheme cannot be evaluated independently from the FSD model; therefore, it does not necessarily mean that each of the individual parameterizations is more realistic. Any improvement in the FSD parameterizations, including the implementation of a universal floe-breaking criterion and a representation of the processes affecting the FSTD over the whole floe size range (0-10 km), will lead to a more realistic MIZ-FSD even with a weaker attenuation scheme.

On the first hand, while the pure strain/stress criterion used in the earlier studies was argued to be adequate as long as we were in the realm of the medium wavelengths (i.e., a wavelength range between $\approx$ 40-400 m), the use of a coupled wave model where the energy spectrum evolves across a broader range of wavelength break that assumption (i.e., a wavelength range between $\approx$ 20-1000 m). In the most general case, neither the stress nor the strain criterion is adequate. A universal criterion should be based on the stress but allow some ice deformation. This way, short wavelengths would be filtered as the moment applied on the beam is too small, and long wavelengths would induce deformation, reducing the load on the plate. Here, the wind input generation term is deactivated to remove high-frequency waves locally generated in a highly concentrated region that can cause unrealistic strain failure where ice is the thickest. However, Cooper et al. (2022) shows that an enhanced wind generation was required to simulate realistic waves in ice spectrum. Such a universal fracture model would reconcile those two results and is subject to future work. Other wave-ice models, such as the one developed in Boutin et al. (2020, 2021) kept the strain criterion but further constrained the breaking threshold by adding a critical diameter and a wave reduction parameter to reduce unrealistic floe breaking, resulting in a MIZ-FSD that is more in line with observations.

On the other hand, the FSTD model has been developed to represent processes at play in the MIZ (in the 0-2 km floe size range) but not in the pack ice (in the 1-10 km floe size range). Observations show that a significant fraction of the MIZ-SIC is also composed of large floes advected from the pack suggesting that the representation of the floe size in the MIZ and the pack ice cannot be considered independently. Our results highlight that one of the critical reasons for the overestimation of the simulated FSD-MIZ is that the presence of a wave field turns off the regrowth of floes. Using the IC4-M8 attenuation scheme, more ice is added to the largest floe size category. However, while it results in a more realistic floe size, this pancake ice formation formulation is not physical and creates thin ice sheets of 2000 m in diameter. In an attempt to facilitate comparison with observations, Horvat et al. (2019) increased the number of FSD categories to 24 (covering the 0-10 km floe size range), but by doing so without modification of the FSTD, they generate pancake ice of 10 km. Including processes at play for larger floe sizes would be a more physical way to better represent the MFD in the pack ice and the MIZ-FSD extent, for example, by representing a generation of large floes in the pack ice based on linear kinematic features instead of pancake ice formation.

Future work includes more comparison of coupled wave-ice models to observations. Recall that the lack of consistent global observation combined with the fact that satellites poorly detect small floes remains a major limitation for precisely validating the simulated FSD in the MIZ. Comparisons with high-resolution images such as the one analyzed in Manucharyan et al. (2022) could help better understand the processes affecting the FSD. Waves in ice observations from satellite or buoys measurement could also be valuable to further constrain the wave attenuation considering the significant uncertainties regarding how waves should be dissipated and generated by the ice cover.

In conclusion, our results helped identify biases associated with the floe size retrieval from the CryoSat-2 satellite altimeter and in the simulated floe size using a fully coupled wave-ice model. It provided further insight into some of the uncertainties and challenges concerning the representation of wave attenuation, wave fracture, and floe size distribution. This testifies to the juvenescence of coupled wave-ice models and that further coordinated efforts, including more observation of the MIZ, are necessary to better constrain the parameterizations. Given the significant role that the Arctic sea-ice cover has in the climate, and considering the projected shift toward a more "MIZ-like" sea-ice cover, such studies are necessary to help improve the understanding of the marginal ice-zone dynamic and improve sea-ice prediction at both short and climatological time scales.

Appendix A

Supplementary material

A.1 Relationship between floe perimeter and floe size

Assuming a circular geometry, the total floe perimeter can be approximated as follows:

$$P_{tot} = N_{floes} \cdot 2\pi\bar{R} = \frac{SIA}{\cancel{\pi}\bar{R}^{\cancel{2}}} 2\cancel{\pi}\cancel{\bar{R}}$$

where $\bar{R}$ is the average radius and N_{floes} is the number of floes in a grid cell, which is given by the sea-ice area (SIA) divided by the average area occupied by a single floe. Replacing the SIA in terms of sea-ice concentration (SIC) and grid area (Δx^2), we have the following expression for the floe perimeter as a function of sea-ice concentration, floe radius, and grid area:

$$P_{tot} = \frac{2\Delta x^2 \; SIC}{\bar{R}}$$

We apply this simple relationship to the SIC and mean floe diameter (MFD) derived from CIS data; this results in a sharp increase in floe perimeter for floe size smaller than 300 m, which further reinforces the choice of the MIZ-FSD criterion (Fig. A.1).

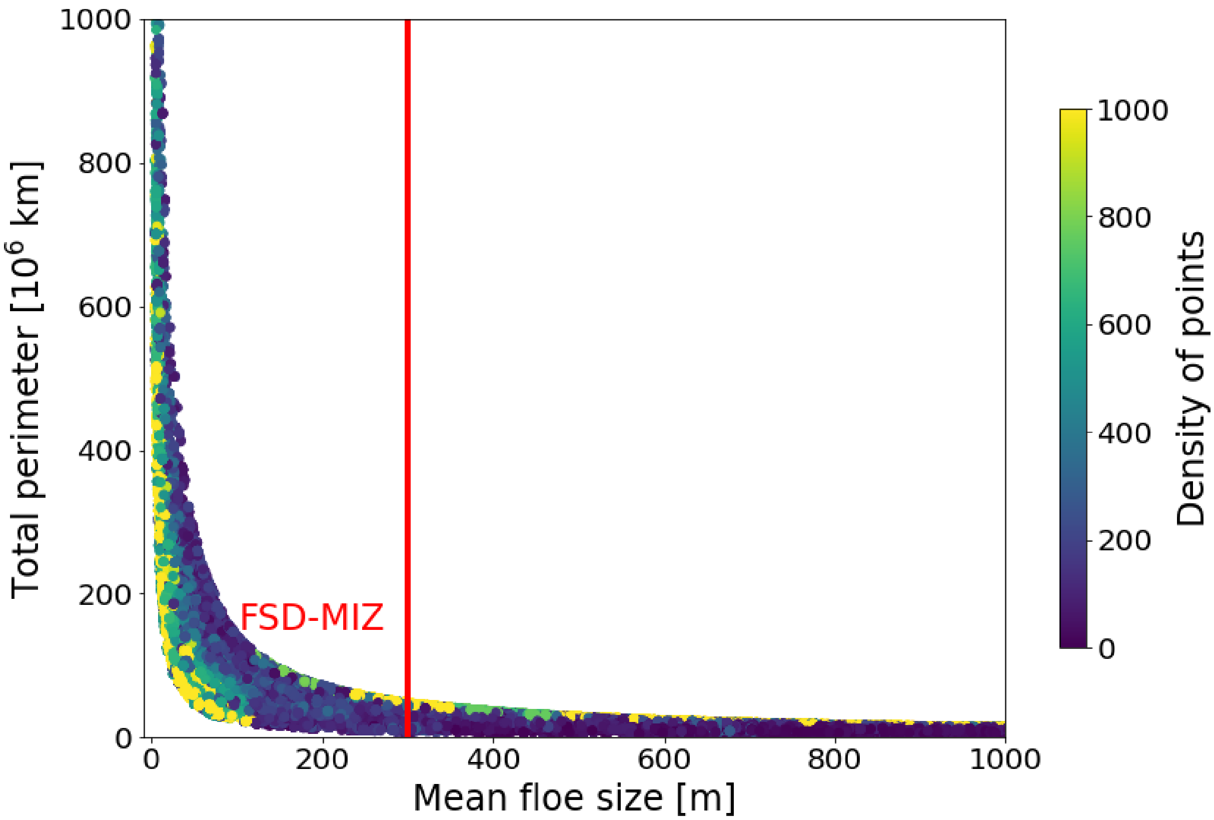

Figure A.1: Relationship between the floe size and perimeter using the 2010-2018 winter CIS data in the Labrador region. The red line shows the FSD-MIZ ($\bar{D} \leq 300$ m) threshold.

Bibliography

A. Alberello, M. Onorato, L. Bennetts, M. Vichi, C. Eayrs, K. Machutchon, and A. Toffoli. Brief communication: Pancake ice floe size distribution during the winter expansion of the antarctic marginal ice zone. *Cryosphere*, 13:41–48, 1 2019. ISSN 19940424. doi: 10.5194/tc-13-41-2019.

M. G. Asplin, R. Galley, D. G. Barber, and S. Prinsenberg. Fracture of summer perennial sea ice by ocean swell as a result of arctic storms. *Journal of Geophysical Research: Oceans*, 117, 2012. ISSN 21699291. doi: 10.1029/2011JC007221.

M. G. Asplin, R. Scharien, B. Else, S. Howell, D. G. Barber, T. Papakyriakou, and S. Prinsenberg. Implications of fractured arctic perennial ice cover on thermodynamic and dynamic sea ice processes. *Journal of Geophysical Research: Oceans*, 119:2327–2343, 2014. ISSN 21699291. doi: 10.1002/2013JC009557.

J.-P. Auclair, D. Dumont, J.-F. Lemieux, and H. Ritchie. A model study of convergent dynamics in the marginal ice zone. *Philosophical Transactions of the Royal Society A: Mathematical, Physical and Engineering Sciences*, 380, 10 2022. ISSN 1364-503X. doi: 10.1098/rsta.2021.0261. URL `https://royalsocietypublishing.org/doi/10.1098/rsta.2021.0261`.

C. M. Bitz, K. M. Shell, P. R. Gent, D. A. Bailey, G. Danabasoglu, K. C. Armour, M. M. Holland, and J. T. Kiehl. Climate sensitivity of the community climate system model, version 4. *Journal of Climate*, 25:3053–3070, 5 2012. ISSN 08948755. doi: 10.1175/JCLI-D-11-00290.1.

G. Boutin, F. Ardhuin, D. Dumont, C. Sévigny, F. Girard-Ardhuin, and M. Accensi. Floe size effect on wave-ice interactions: Possible effects, implementation in wave model, and evaluation. *Journal of Geophysical Research: Oceans*, 123:4779–4805, 7 2018. ISSN 21699291. doi: 10.1029/2017JC013622.

G. Boutin, C. Lique, F. Ardhuin, C. Rousset, C. Talandier, M. Accensi, and F. Girard-Ardhuin. Towards a coupled model to investigate wave-sea ice interactions in the arctic marginal ice zone. *Cryosphere*, 14:709–735, 3 2020. ISSN 19940424. doi: 10.5194/tc-14-709-2020.

G. Boutin, T. Williams, P. Rampal, E. Olason, and C. Lique. Wave-sea-ice interactions in a brittle rheological framework. *Cryosphere*, 15:431–457, 1 2021. ISSN 19940424. doi: 10.5194/tc-15-431-2021.

G. Boutin, T. Williams, C. Horvat, and L. Brodeau. Modelling the arctic wave-affected marginal ice zone: a comparison with icesat-2 observations. *Philosophical Transactions of the Royal Society A: Mathematical, Physical and Engineering Sciences*, 380, 10 2022. ISSN 1364-503X. doi: 10.1098/rsta.2021.0262. URL `https://royalsocietypublishing.org/doi/10.1098/rsta.2021.0262`.

T. Browne, D. Watson, J. Broderick, and M. Sayed. Analysis of pack ice deterioration due to wave action on the grand banks. *Conference on Port and Ocean Engineering under Arctic Conditions*, 6 2017. URL `https://www.researchgate.net/publication/339723569`.

M. Casas-Prat and X. L. Wang. Sea ice retreat contributes to projected increases in extreme arctic ocean surface waves. *Geophysical Research Letters*, 47, 8 2020. ISSN 19448007. doi: 10.1029/2020GL088100.

C. O. Collins, W. E. Rogers, and B. Lund. An investigation into the dispersion of ocean surface waves in sea ice. *Ocean Dynamics*, 67:263–280, 2 2017. ISSN 16167228. doi: 10.1007/s10236-016-1021-4.

V. T. Cooper, L. A. Roach, J. Thomson, S. D. Brenner, M. M. Smith, M. H. Meylan, and C. M. Bitz. Wind waves in sea ice of the western arctic and a global coupled wave-ice model. *Philosophical Transactions of the Royal Society A: Mathematical, Physical and Engineering Sciences*, 380, 10 2022. ISSN 1364503X. doi: 10.1098/rsta.2021.0258.

N. DiGirolamo, C. L. Parkinson, D. J. Cavalieri, P. Gloersen, and H. J. Zwally. Sea ice concentrations from nimbus-7 smmr and dmsp ssm/i-ssmis passive microwave data, version 2, 2022. URL `https://nsidc.org/data/NSIDC-0051/versions/2`.

D. Dumont, A. Kohout, and L. Bertino. A wave-based model for the marginal ice zone including a floe breaking parameterization. *Journal of Geophysical Research: Oceans*, 116, 2011. ISSN 21699291. doi: 10.1029/2010JC006682.

ECCC. Ice climate normals for the northern canadian waters 1991 to 2020, Jun 2022. URL `https://www.canada.ca/en/environment-climate-change/services/ice-forecasts-observations/latest-conditions/climatology/ice-climate-normals/canadian-east-coast-waters.html`.

D. L. Feltham, N. Untersteiner, J. S. Wettlaufer, and M. G. Worster. Sea ice is a mushy layer. *Geophysical Research Letters*, 33, 7 2006. ISSN 00948276. doi: 10.1029/2006GL026290.

C. Fox and A. V. Squire. On the oblique reflexion and transmission of ocean waves at shore fast sea ice. *Philosophical Transactions of the Royal Society A: Mathematical, Physical and Engineering Sciences*, 347, 1994. URL `https://royalsocietypublishing.org/`.

C. Horvat. Floes, the marginal ice zone and coupled wave-sea-ice feedbacks, 10 2022. ISSN 1364503X.

C. Horvat and L. A. Roach. Wiff1.0: A hybrid machine-learning-based parameterization of wave-induced sea ice floe fracture. *Geoscientific Model Development*, 15:803–814, 1 2022. ISSN 19919603. doi: 10.5194/gmd-15-803-2022.

C. Horvat and E. Tziperman. A prognostic model of the sea-ice floe size and thickness distribution. *Cryosphere*, 9:2119–2134, 11 2015. ISSN 19940424. doi: 10.5194/tc-9-2119-2015.

C. Horvat, L. A. Roach, R. Tilling, C. M. Bitz, B. Fox-Kemper, C. Guider, K. Hill, A. Ridout, and A. Shepherd. Estimating the sea ice floe size distribution using satellite altimetry: Theory, climatology, and model comparison. *Cryosphere*, 13:2869–2885, 11 2019. ISSN 19940424. doi: 10.5194/tc-13-2869-2019.

E. Hunke, R. Allard, D. A. Bailey, P. Blain, A. Craig, F. Dupont, A. DuVivier, R. Grumbine, D. Hebert, M. Holland, N. Jeffery, J.-F. Lemieux, R. Osinski, T. Rasmussen, M. Ribergaard, L. Roach, A. Roberts, M. Turner, and M. Winton. Cice-consortium/icepack: Icepack 1.3.3, Dec. 2022a. URL `https://doi.org/10.5281/zenodo.7419438`.

E. Hunke, R. Allard, D. A. Bailey, P. Blain, A. Craig, F. Dupont, A. DuVivier, R. Grumbine, D. Hebert, M. Holland, N. Jeffery, J.-F. Lemieux, R. Osinski, T. Rasmussen, M. Ribergaard, L. Roach, A. Roberts, M. Turner, M. Winton, and D. Worthen. Cice-consortium/cice: Cice version 6.4.1, Dec. 2022b. URL `https://doi.org/10.5281/zenodo.7419531`.

E. C. Hunke, D. A. Hebert, and O. Lecomte. Level-ice melt ponds in the los alamos sea ice model, cice. *Ocean Modelling*, 71:26–42, 11 2013. ISSN 14635003. doi: 10.1016/j.ocemod.2012.11.008.

A. Jahn. Reduced probability of ice-free summers for 1.5 °c compared to 2 °c warming. *Nature Climate Change*, 8:409–413, 5 2018. ISSN 17586798. doi: 10.1038/s41558-018-0127-8.

J. E. Kay, C. Deser, A. Phillips, A. Mai, C. Hannay, G. Strand, J. M. Arblaster, S. C. Bates, G. Danabasoglu, J. Edwards, M. Holland, P. Kushner, J. F. Lamarque, D. Lawrence, K. Lindsay, A. Middleton, E. Munoz, R. Neale, K. Oleson, L. Polvani, and M. Vertenstein. The community earth system model (cesm) large ensemble project : A community resource for studying climate change in the presence of internal climate variability.

Bulletin of the American Meteorological Society, 96:1333–1349, 8 2015. ISSN 15200477. doi: 10.1175/BAMS-D-13-00255.1.

J. B. Keller. Gravity waves on ice-covered water. *Journal of Geophysical Research: Oceans*, 103:7663–7669, 1998. ISSN 21699291. doi: 10.1029/97jc02966.

S. Kern, T. Lavergne, D. Notz, L. T. Pedersen, and R. Tonboe. Satellite passive microwave sea-ice concentration data set inter-comparison for arctic summer conditions. *Cryosphere*, 14:2469–2493, 7 2020. ISSN 19940424. doi: 10.5194/tc-14-2469-2020.

S. Kobayashi, Y. Ota, Y. Harada, A. Ebita, M. Moriya, H. Onoda, K. Onogi, H. Kamahori, C. Kobayashi, H. Endo, K. Miyaoka, and T. Kiyotoshi. The jra-55 reanalysis: General specifications and basic characteristics. *Journal of the Meteorological Society of Japan*, 93: 5–48, 3 2015. ISSN 00261165. doi: 10.2151/jmsj.2015-001.

A. L. Kohout and M. H. Meylan. An elastic plate model for wave attenuation and ice floe breaking in the marginal ice zone. *Journal of Geophysical Research: Oceans*, 113, 9 2008. ISSN 21699291. doi: 10.1029/2007JC004434.

A. L. Kohout, M. J. Williams, S. M. Dean, and M. H. Meylan. Storm-induced sea-ice breakup and the implications for ice extent. *Nature*, 509:604–607, 2014. ISSN 14764687. doi: 10.1038/nature13262.

R. Kwok. Arctic sea ice thickness, volume, and multiyear ice coverage: Losses and coupled variability (1958-2018), 10 2018. ISSN 17489326.

A. LeGuern-Lepage and B. Tremblay. *A likely mechanism for a "first-time" ice-free Arctic*. Msc. thesis, McGill University, Montreal, Canada, August 2022. Available at `https://escholarship.mcgill.ca/concern/theses/5138jk65r`.

J. Li, Y. Ma, Q. Liu, W. Zhang, and C. Guan. Growth of wave height with retreating ice cover in the arctic. *Cold Regions Science and Technology*, 164, 8 2019. ISSN 0165232X. doi: 10.1016/j.coldregions.2019.102790.

A. K. Liu and E. Mollo-Christensen. Wave propagation in a solid ice pack. *Journal of Physical Oceanography*, 18:1702–1712, 1988.

A. K. Liu, S. Hakkinen, and Y. P. Chih. Wave effects on ocean-ice interaction in the marginal ice zone. *Journal of Geophysical Research*, 98, 1993. ISSN 01480227. doi: 10.1029/93jc00653.

Q. Liu, A. V. Babanin, S. Zieger, I. R. Young, and C. Guan. Wind and wave climate in the arctic ocean as observed by altimeters. *Journal of Climate*, 29:7957–7975, 2016. ISSN 08948755. doi: 10.1175/JCLI-D-16-0219.1.

M. S. Longuet-Higgins and R. W. Stewart. Radiation stresses in vater waves; a physical discussion, with applications, 1964.

G. E. Manucharyan, R. Lopez-Acosta, and M. M. Wilhelmus. Spinning ice floes reveal intensification of mesoscale eddies in the western arctic ocean. *Scientific Reports*, 12, 12 2022. ISSN 20452322. doi: 10.1038/s41598-022-10712-z.

M. H. Meylan and L. G. Bennetts. Three-dimensional time-domain scattering of waves in the marginal ice zone. *Philosophical Transactions of the Royal Society A: Mathematical, Physical and Engineering Sciences*, 376, 9 2018. ISSN 1364503X. doi: 10.1098/rsta.2017.0334.

M. H. Meylan and D. Masson. A linear boltzmann equation to model wave scattering in the marginal ice zone. *Ocean Modelling*, 11:417–427, 2006. ISSN 14635003. doi: 10.1016/j.ocemod.2004.12.008.

M. H. Meylan, L. G. Bennetts, and A. L. Kohout. In situ measurements and analysis of ocean waves in the antarctic marginal ice zone. *Geophysical Research Letters*, 41:5046–5051, 7 2014. ISSN 19448007. doi: 10.1002/2014GL060809.

M. H. Meylan, C. Horvat, C. M. Bitz, and L. G. Bennetts. A floe size dependent scattering model in two- and three-dimensions for wave attenuation by ice floes. *Ocean Modelling*, 161, 5 2021. ISSN 14635003. doi: 10.1016/j.ocemod.2021.101779.

F. Montiel, V. A. Squire, and L. G. Bennetts. Attenuation and directional spreading of ocean wave spectra in the marginal ice zone. *Journal of Fluid Mechanics*, 790:492–522, 2 2016. ISSN 14697645. doi: 10.1017/jfm.2016.21.

J. E. Mosig, F. Montiel, and V. A. Squire. Comparison of viscoelastic-type models for ocean wave attenuation in ice-covered seas. *Journal of Geophysical Research: Oceans*, 120: 6072–6090, 9 2015. ISSN 21699291. doi: 10.1002/2015JC010881.

J. E. Overland and M. Wang. When will the summer arctic be nearly sea ice free? *Geophysical Research Letters*, 40:2097–2101, 5 2013. ISSN 00948276. doi: 10.1002/grl.50316.

C. L. Parkinson and J. C. Comiso. On the 2012 record low arctic sea ice cover: Combined impact of preconditioning and an august storm. *Geophysical Research Letters*, 40:1356–1361, 4 2013. ISSN 00948276. doi: 10.1002/grl.50349.

D. K. Perovich and K. F. Jones. The seasonal evolution of sea ice floe size distribution. *Journal of Geophysical Research: Oceans*, 119:8767–8777, 12 2014. ISSN 21699291. doi: 10.1002/2014JC010136.

D. K. Perovich, J. A. Richeter-Menge, K. F. Jones, and B. Light. Sunlight, water, and ice: Extreme arctic sea ice melt during the summer of 2007. *Geophysical Research Letters*, 35, 6 2008. ISSN 00948276. doi: 10.1029/2008GL034007.

M. Rantanen, A. Y. Karpechko, A. Lipponen, K. Nordling, O. Hyvärinen, K. Ruosteenoja, T. Vihma, and A. Laaksonen. The arctic has warmed nearly four times faster than the globe since 1979. *Communications Earth and Environment*, 3, 12 2022. ISSN 26624435. doi: 10.1038/s43247-022-00498-3.

L. A. Roach, M. M. Smith, and S. M. Dean. Quantifying growth of pancake sea ice floes using images from drifting buoys. *Journal of Geophysical Research: Oceans*, 123:2851–2866, 4 2018. ISSN 21699291. doi: 10.1002/2017JC013693.

L. A. Roach, C. M. Bitz, C. Horvat, and S. M. Dean. Advances in modeling interactions between sea ice and ocean surface waves. *Journal of Advances in Modeling Earth Systems*, 11:4167–4181, 12 2019. ISSN 19422466. doi: 10.1029/2019MS001836.

E. Rogers. A source term for wave attenuation by sea ice in wavewatch iii ® : Ic4, 2017.

H. H. Shen. Modelling ocean waves in ice-covered seas, 2 2019. ISSN 01411187.

H. H. Shen. Wave-in-ice: theoretical bases and field observations. *Philosophical Transactions of the Royal Society A: Mathematical, Physical and Engineering Sciences*, 380, 10 2022. ISSN 1364503X. doi: 10.1098/rsta.2021.0254.

Q. Shu, Q. Wang, Z. Song, F. Qiao, J. Zhao, M. Chu, and X. Li. Assessment of sea ice extent in cmip6 with comparison to observations and cmip5. *Geophysical Research Letters*, 47, 5 2020. ISSN 19448007. doi: 10.1029/2020GL087965.

V. A. Squire. Of ocean waves and sea-ice revisited. *Cold Regions Science and Technology*, 49: 110–133, 8 2007. ISSN 0165232X. doi: 10.1016/j.coldregions.2007.04.007.

V. A. Squire. Ocean wave interactions with sea ice: A reappraisal. 2020. doi: 10.1146/annurev-fluid-010719. URL `https://doi.org/10.1146/annurev-fluid-010719-`.

V. A. Squire. Marginal ice zone dynamics, 10 2022. ISSN 1364503X.

V. A. Squire and S. C. Moore. Direct measurement of the attenuation of ocean waves by pack ice. 1980.

M. Steele. Sea ice melting and floe geometry in a simple ice-ocean model. *Journal of Geophysical Research*, 97, 1992. ISSN 01480227. doi: 10.1029/92jc01755.

H. L. Stern, A. J. Schweiger, J. Zhang, and M. Steele. On reconciling disparate studies of the sea-ice floe size distribution. *Elementa: Science of the Anthropocene*, 6, 2018. doi: 10.1525/elementa.304.t1. URL https://doi.org/10.1525/elementa.304.t1.

J. E. Stopa, P. Sutherland, and F. Ardhuin. Strong and highly variable push of ocean waves on southern ocean sea ice. *Proceedings of the National Academy of Sciences of the United States of America*, 115:5861–5865, 6 2018. ISSN 10916490. doi: 10.1073/pnas.1802011115.

J. Stroeve and D. Notz. Changing state of arctic sea ice across all seasons, 9 2018. ISSN 17489326.

C. Strong. Atmospheric influence on arctic marginal ice zone position and width in the atlantic sector, february-april 1979-2010. *Climate Dynamics*, 39:3091–3102, 11 2012. ISSN 09307575. doi: 10.1007/s00382-012-1356-6.

C. Strong and I. G. Rigor. Arctic marginal ice zone trending wider in summer and narrower in winter. *Geophysical Research Letters*, 40:4864–4868, 9 2013. ISSN 00948276. doi: 10.1002/grl.50928.

P. Sutherland and D. Dumont. Marginal ice zone thickness and extent due to wave radiation stress. *Journal of Physical Oceanography*, 48:1885–1901, 8 2018. ISSN 15200485. doi: 10.1175/JPO-D-17-0167.1.

J. Thomson and W. E. Rogers. Swell and sea in the emerging arctic ocean. *Geophysical Research Letters*, 41:3136–3140, 5 2014. ISSN 19448007. doi: 10.1002/2014GL059983.

T. Toyota, S. Takatsuji, and M. Nakayama. Characteristics of sea ice floe size distribution in the seasonal ice zone. *Geophysical Research Letters*, 33, 1 2006. ISSN 00948276. doi: 10.1029/2005GL024556.

T. Toyota, C. Haas, and T. Tamura. Size distribution and shape properties of relatively small sea-ice floes in the antarctic marginal ice zone in late winter. *Deep-Sea Research*

Part II: Topical Studies in Oceanography, 58:1182–1193, 5 2011. ISSN 09670645. doi: 10.1016/j.dsr2.2010.10.034.

M. Tsamados, D. Feltham, A. Petty, D. Schroeder, and D. Flocco. Processes controlling surface, bottom and lateral melt of arctic sea ice in a state of the art sea icemodel. *Philosophical Transactions of the Royal Society A: Mathematical, Physical and Engineering Sciences*, 373, 10 2015. ISSN 1364503X. doi: 10.1098/rsta.2014.0167.

A. K. Turner, E. C. Hunke, and C. M. Bitz. Two modes of sea-ice gravity drainage: A parameterization for large-scale modeling. *Journal of Geophysical Research: Oceans*, 118: 2279–2294, 5 2013. ISSN 21699291. doi: 10.1002/jgrc.20171.

P. Wadhams, V. A. Squire, D. J. Goodman, A. M. Cowan, and S. C. Moore. The attenuation rates of ocean waves in the marginal ice zone. *Journal of Geophysical Research*, 93:6799, 1988. ISSN 0148-0227. doi: 10.1029/jc093ic06p06799.

M. Wang and J. E. Overland. A sea ice free summer arctic within 30 years: An update from cmip5 models. *Geophysical Research Letters*, 39, 9 2012. ISSN 00948276. doi: 10.1029/2012GL052868.

R. Wang and H. H. Shen. Gravity waves propagating into an ice-covered ocean: A viscoelastic model. *Journal of Geophysical Research: Oceans*, 115, 2010. ISSN 21699291. doi: 10.1029/2009JC005591.

T. D. Williams, L. G. Bennetts, V. A. Squire, D. Dumont, and L. Bertino. Wave-ice interactions in the marginal ice zone. part 1: Theoretical foundations. *Ocean Modelling*, 71: 81–91, 11 2013. ISSN 14635003. doi: 10.1016/j.ocemod.2013.05.010.

T. D. Williams, P. Rampal, and S. Bouillon. Wave-ice interactions in the nextsim sea-ice model. *Cryosphere*, 11:2117–2135, 9 2017. ISSN 19940424. doi: 10.5194/tc-11-2117-2017.

WW3DG. User Manual and System Documentation of WAVEWATCH III version 6.07, The WAVEWATCH III Development Group. *Tech. Note 326 pp. + Appendices, NOAA/NWS/NCEP/MMAB*, 2019.

J. Zhang, H. Stern, B. Hwang, A. Schweiger, M. Steele, M. Stark, and H. C. Graber. Modeling the seasonal evolution of the arctic sea ice floe size distribution. *Elementa*, 4, 2016. ISSN 23251026. doi: 10.12952/journal.elementa.000126.